
Cross-Chirality Generalization by Axial Vectors for Hetero-Chiral Protein-Peptide Interaction Design

Ziyi Yang^{*1} Zitong Tian^{*2} Yinjun Jia^{*3} Tianyi Zhang¹ Jiqing Zheng¹ Hao Wang¹ Yubu Su¹ Juncai He^{2,4}
Lei Liu^{1,5,6,7} Yanyan Lan^{3,8}

Abstract

D-peptide binders targeting L-proteins have promising therapeutic potential. Despite rapid advances in machine learning-based target-conditioned peptide design, generating D-peptide binders remains largely unexplored. In this work, we show that by injecting axial features to $E(3)$ -equivariant (polar) vector features, it is feasible to achieve cross-chirality generalization from homo-chiral (L-L) training data to hetero-chiral (D-L) design tasks. By implementing this method within a latent diffusion model, we achieved D-peptide binder design that not only outperforms existing tools in *in silico* benchmarks, but also demonstrates efficacy in wet-lab validation. To our knowledge, our approach represents the first wet-lab validated generative AI for the *de novo* design of D-peptide binders, offering new perspectives on handling chirality in protein design.

1. Introduction

A hallmark of proteins is their homo-chirality: nature predominantly uses L-amino acids to construct proteins within living organisms (Pasteur, 1848; Blackmond, 2010). In this context, D-peptides become advantaged molecules for therapeutics due to their intrinsic orthogonality in an all-L system. D-peptides cannot be recognized as substrates

by proteases, thereby exhibiting prolonged *in vivo* half-life (Kremsmayr et al., 2022). Besides, the bioorthogonality of D-peptides reduces their immunogenicity and risks of drug-drug interactions (DDI) (Lander et al., 2023; Qi et al., 2024). Conventionally, D-peptide binders are identified via mirror-image display, where D-protein targets are synthesized for L-peptide binder screening. Once an L-peptide is identified, its mirror-image counterpart will inherently bind to the natural protein, thus yielding a D-peptide binder (Qi et al., 2024; Chang et al., 2015; Zhou et al., 2020). However, the difficulties of D-protein target synthesis limited its application to most real-world drug discovery.

Recently, machine learning-based peptide binder design has been proven practical, and has shown advantages including the specificity to certain epitopes, higher success rate, lower screening cost, and more diverse initial scaffolds for affinity maturation and property optimization (Kong et al., 2025a; Notin et al., 2024). However, current works mainly focus on designing L-L homo-chiral interfaces, while generating D-L hetero-chiral interactions remains largely unexplored. Best to our knowledge, D-Flow (Wu et al., 2024) is the only AI exploration of this topic, which lacks further experimental validation.

In this work, we theoretically analyze the zero-shot cross-chirality generation task for scalarization-based equivariant model (Han et al., 2025). We show that by injecting axial features to polar vector features in geometric neural networks, residues with different chirality will have different but similar latent representations, allowing chirality awareness and cross-chirality generalization. By implementing this in a latent diffusion model, we build PepMirror, the state of the art (SOTA) D-peptide binder *de novo* design model as shown by both *in-silico* and *in-vitro* experiments in wetlabs. In short, our main contributions include:

- (1) We propose AFI (Axial Feature Injection), a plug-and-play method to make an $E(3)$ -equivariant model to chirality-sensitive (only $SE(3)$ -equivariant).
- (2) To understand AFI, we provide theoretical analysis together with numerical validation on the AFI-using encoder model by latent space analysis.

^{*}Equal contribution ¹Department of Chemistry, Tsinghua University, Beijing, China ²QiuZhen College, Tsinghua University, Beijing, China ³Institute for AI Industry Research (AIR), Tsinghua University, Beijing, China ⁴Yau Mathematical Sciences Center, Tsinghua University, Beijing, China ⁵Tsinghua-Peking Center for Life Sciences, Beijing, China ⁶Ministry of Education Key Laboratory of Bioorganic Phosphorus Chemistry and Chemical Biology, Tsinghua University, Beijing, China ⁷Center for Synthetic and Systems Biology, Tsinghua University, Beijing, China ⁸Beijing Frontier Research Center for Biological Structure, Tsinghua University, Beijing, China. Correspondence to: Juncai He <jche@tsinghua.edu.cn>, Lei Liu <liliu@mail.tsinghua.edu.cn>, Yanyan Lan <lanyanyan@air.tsinghua.edu.cn>.

(3) Based on AFI, we present PepMirror, an experimentally validated *de novo* framework for mirror-image peptide binder design, supported by comprehensive dry-lab evaluation and wet-lab validation.

2. Related Works

Chirality in protein models A popular paradigm in protein models is to represent each residue with a local rigid-body frame, parameterized by a translation vector and a rotation matrix from the global frame to the local frame. This method was adopted by many protein structure prediction models such as AlphaFold2 (Jumper et al., 2021), and also many peptide generative models including RFDiffusion (Watson et al., 2023), DiffPepBuilder (Wang et al., 2024), PepFlow (Li et al., 2024), PPFlow (Lin et al., 2024), PepBridge (Li et al., 2025a), D-Flow (Wu et al., 2024), etc. In these models, the chirality of residues is fixed by the definition of the rigid-body and local frames are designed to be right-handed. As a result, a residue and its mirror-image structure will have different rotation matrix but are not in a reflection relationship. In other words, chirality is implicitly encoded as a prior, and the parameterization is reflection-agnostic.

Alternatively, some models parameterize proteins without explicit chirality priors. For instance, PepGLAD (Kong et al., 2025a) and UniMoMo (Kong et al., 2025b) utilize residue-level latent features, FuncBind (Kirchmeyer et al., 2025) employs neural fields to represent atoms as density peaks, PocketXMol (Peng et al., 2025) employs full-atom diffusion, in which chirality is represented only implicitly through atomic coordinates. As these models typically rely on $E(3)$ -equivariant architectures, they are inherently restricted to generating homo-chiral complexes (i.e., L-L or D-D protein-peptide pairs as observed in the training data) unless additional chirality-specific features are introduced. Furthermore, because chirality is not modeled explicitly, the generated peptide ligands frequently exhibit varying degrees of residue-level chirality inversion (Table 1).

Chirality aware models in geometric learning There have been multiple approaches to encode chirality of a structure in geometric learning. Representative examples include adding chiral tags in node features (e.g., ChiralCliff (Schneider et al., 2018)), injecting torsions in message passing (e.g., SphereNet (Coors et al., 2018)) or using coupled torsions and aggregates them with a learnable phase shift to disentangle conformation changes and chirality shifts (e.g., ChIRo (Adams et al., 2021)), designing shift-equivariant yet order-sensitive aggregations (e.g., ChiENN (Gaiński et al., 2023) and Tetra-DMPNN (Du et al., 2024)), and introducing parity-even channels such as pseudovectors and mixing them with parity-odd features (e.g., GCPNet (Morehead & Cheng,

2024), REM3DI (Wedig et al., 2025)). Although these architectures have been proved effective for tasks like chirality classification and molecular property prediction, they have not been applied in designing hetero-chiral peptide-protein interfaces.

Representation theory and chiral features Equivariant networks grounded in representation theory, such as Tensor Field Networks (Thomas et al., 2018), $SE(3)$ -Transformers (Fuchs et al., 2020), and e3nn (Geiger & Smidt, 2022), leverage spherical harmonics and tensors to encode rich geometric interactions. While highly expressive (Smidt et al., 2021), these models incur significantly higher computational costs (Li et al., 2025b) compared to standard $E(3)$ Graph Neural Networks (Satorras et al., 2022). In contrast, we introduce a lightweight axial feature injection that incorporates chirality into efficient $E(3)$ backbones with minimal architectural changes.

Design D-peptides as L-protein binders Early efforts on hetero-chiral binder design are mainly based on molecular mechanics, employing methods including the RifGen-RifDock-Rosetta pipeline (Cao et al., 2022; Sun et al., 2024) and fragments assembly approaches (Garton et al., 2018; Engel et al., 2021), which suffer from low success rates, and always need large-scale library screening to identify active molecules. Recently, designing protein-binding proteins based on machine learning has been extensively explored, but few models involve mirror-image peptides. To our knowledge, the only attempt to design D-peptide binders is reported in D-Flow (Wu et al., 2024), where a similar workflow to mirror-image display is utilized.

3. Method

3.1. Preliminary

A protein can be regarded as a point cloud graph \mathcal{G} of the 3D atom coordinates and atom-types. Inspired by mirror-image display and D-Flow (Wu et al., 2024), a D-peptide binder can be generated by two-step inversion. The L-protein target \mathcal{G}_t can be first inverted to its mirror-image counterpart $\mathcal{G}'_t = P(\mathcal{G}_t)$, where P is the spatial inversion on atoms coordinates: $P = -I_3 \in O(3) \setminus SO(3)$. Then, if the generative model designs an L-peptide binder \mathcal{G}_b against this D-target \mathcal{G}'_t , the inverted version of \mathcal{G}_b would be the D-peptide binder for the L-target, and these two binder-target pairs should have the same affinity under P . Formally, the desired D-peptide binder is $\mathcal{G}_b = P(f_\theta(P(\mathcal{G}_t)))$, where $f_\theta(x)$ denotes the model parameterized by θ that generates a peptide binder graph conditioned on x .

A popular instantiation of f_θ is a scalarization-based $E(3)$ -equivariant model (Han et al., 2025; Satorras et al., 2022), where a 3D object X is embedded as $(H(X), V(X))$,

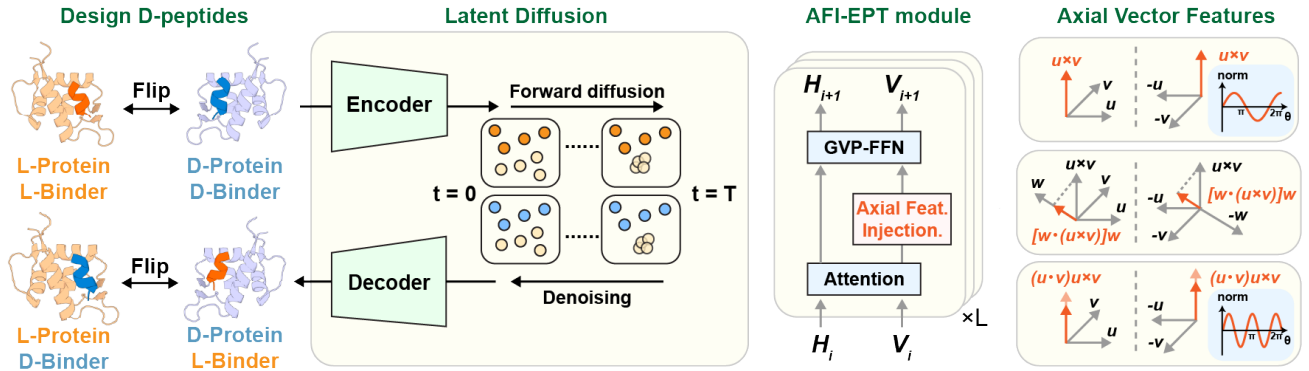


Figure 1. We use chiral-sensitive model PepMirror to design D-peptides by flipping. PepMirror is a latent diffusion model using AFI-EPT, which injects axial vector features to learn the chirality. Axial vectors are invariant under the spatial inversion, and we give three direct constructions. The commutator feature (third) captures higher frequency information of the angle between u, v .

where $H(X) \in \mathbb{R}^{N \times K}$ denotes the $E(3)$ -invariant scalar features and $V(X) \in \mathbb{R}^{N \times 3 \times K}$ the $E(3)$ -equivariant vector features, K is the number of channels. The neural network updates (H, V) jointly.

3.2. Hetero-chiral design as a zero-shot generalization

Due to the homo-chiral feature of native proteins, experimentally resolved structures for hetero-chiral protein-protein interactions are scarce. As a result, peptide generation conditioned on targets of different chirality becomes a zero-shot generalization problem: the model is trained on homo-chiral complexes, yet the tasks are under unseen hetero-chiral conditions.

This problem calls for two properties. First, the model must be *chirality-aware*. Second, the representation should remain stable under spatial inversion: for any amino acid X , the code of its mirror image $-X$ should stay within the same amino-acid type (differing only by chirality), rather than collapsing or drifting toward other types.

3.3. Chirality awareness by introducing axial vectors

To make the equivariant model chirality awareness, we need to break the inversion equivariance of vector features and keep the $SE(3)$ -equivariant at the same time.

We introduce *axial vector*, satisfying

$$a(Rx) = \det(R) R a(x), \quad \forall R \in O(3). \quad (1)$$

Accordingly, *polar vector* is $E(3)$ -equivariant. Vector features in vanilla scalarization-based $E(3)$ models are polar vector features. We follow standard terminology in classical physics (Jackson, 2021). Common examples include position and velocity (polar vectors), as opposed to angular momentum and magnetic fields (axial vectors). We propose *Axial Feature Injection* (AFI) by adding axial features to the original polar features by channel wise linear mixing. For

$i = 1, \dots, N, k = 1, \dots, K$, define the new mixed feature

$$\tilde{v}_{i,k}(X) := A_k^\top v_{i,:}(X) + B_k^\top a_{i,:}(X), \quad (2)$$

where $A_k, B_k \in \mathbb{R}^K$ are channel-wise mixing coefficients.

We study the mechanism of AFI by applying an MLP φ to the invariant features and the vector norm channel-wise

$$c(X) = \varphi([\|H(X)\|, \|\tilde{V}(X)\|]), \quad (3)$$

where the norm is computed over 3d spacial dimension, and

$$\tilde{V}(X) = A^\top v(X) + B^\top a(X) \in \mathbb{R}^{N \times 3 \times K} \quad (4)$$

is the mixed vector features.

Under some boundedness assumptions on vector features and probability assumptions on mixing parameters, we can prove 3.1 (see the formal version and proof at Theorem B.8 and Corollary B.9).

Theorem 3.1 (Chirality awareness, informal). *For a sample of amino acid X , under some mild assumptions, we have for any $\varepsilon \in (0, 1)$, with probability at least $1 - \delta_W(\varepsilon)$,*

$$\|c(X) - c(-X)\| \geq c_W \varepsilon, \quad (5)$$

where c_W is a constant.

We remark that the existence of a chirality-induced discrepancy is not automatic, even with axial feature injection (AFI). First, if $B = 0$, the model reduces to an $E(3)$ -equivariant architecture, hence no discrepancy (cf. Proposition 3.2). Second, even when axial channels are present, certain (non-generic) mixing configurations can eliminate the discrepancy. Take $A = B = I$, and for simplicity we omit the indices i, k , then $\tilde{v}(X) = v(X) + a(X)$ and $\tilde{v}(-X) = -v(X) + a(X)$. Hence

$$\|\tilde{v}(-X)\| = \|-v(X) + a(X)\| \quad (6)$$

$$\stackrel{*}{=} \|v(X) + a(X)\| = \|\tilde{v}(X)\|, \quad (7)$$

where $*$ holds whenever $v(X) \cdot a(X) = 0$. This orthogonality can indeed occur in structured settings (e.g., when a contains cross-product terms as two cases in our implementation, see Section 3.5). Therefore, one should not expect a uniform deterministic lower bound over all parameter choices. Instead, our theorems establish a *generic* guarantee: the learned parameters fall into the discrepancy-inducing regime with high probability.

Without AFI, the model is equivariant under spatial inversion. By definition, we can prove that absence of AFI implies no discrepancy even for multi-layer models.

Proposition 3.2 (No discrepancy without AFI). *In the absence of AFI i.e., when using only $E(3)$ -equivariant Neural Networks, then we have $c(X) = c(-X)$.*

Proof. For $j = 1, \dots, L$, We denote the features at layer j as $(H_j(X), V_j(X))$. Under the spatial inversion, by the equivariant property, $(H_j(-X), V_j(-X)) = (H_j(X), -V_j(X))$. The scalar output is

$$c(-X) = \varphi(\|H_L(X), -V_L(X)\|) \quad (8)$$

$$= \varphi(\|H_L(X), \|V_L(X)\|) = c(X). \quad (9)$$

Though the chirality awareness is theoretically analyzed only for AFI, we observe a similar nontrivial effect in the full multi-layer model. See Fig. 3 and Section 4.1.

3.4. Stable representations for enantiomer structures

Encoding stability Although a nontrivial discrepancy is observed under spatial inversion, $c(X)$ and $c(-X)$ represent the same amino-acid type and differ only by chirality. We abstract the multilayer equivariant model as a map ϕ and define the latent code by

$$c(X) = \phi(H(X), \tilde{V}(X)), \tilde{V}(X) := \{\tilde{v}_{i,k}(X)\}_{i,k}, \quad (10)$$

where $H(X)$ and $\tilde{V}(X)$ denote the scalar and vector graph embeddings (see Appendix B.5). To compare molecules with different sizes, we apply zero-padding to align dimensions and define the embedding-space discrepancy

$$d(X_1, X_2) := \|H(X_1) - H(X_2)\| + \|\tilde{V}(X_1) - \tilde{V}(X_2)\|. \quad (11)$$

The embedding satisfies $H(-X) = H(X)$, and AFI yields $a(-X) = a(X)$ while $v(-X) = -v(X)$. Hence the change from X to its mirror image $-X$ is confined to the polar contribution, and in particular

$$d(X, -X) = \|\tilde{V}(X) - \tilde{V}(-X)\| \quad (12)$$

$$= \|2A v(X)\|, \quad (13)$$

where A, B denote the channel-mixing coefficients in Eq. (2).

For an amino acid X' of a different type, both the scalar embedding H and the vector embedding \tilde{V} are expected to differ substantially, with no symmetry-induced cancellation. We therefore assume the embedding-level separation

$$d(X, X') > d(X, -X). \quad (14)$$

Such assumption can be supported by computing the Tanimoto shape similarity between amino acid pairs, see Fig. 2. While X does not admit a direct correspondence to molecular shape, both are geometry-derived representations. Therefore, the result provides an indirect, geometric corroboration of this assumption.

If ϕ preserves this ordering in the sense that larger embedding discrepancies lead to larger code discrepancies, then it follows that

$$\|c(X) - c(-X)\| < \|c(X) - c(X')\|. \quad (15)$$

This provides a simple geometric explanation for the observed 20-clusters phenomenon, see Fig. 4 and Section 4.1.

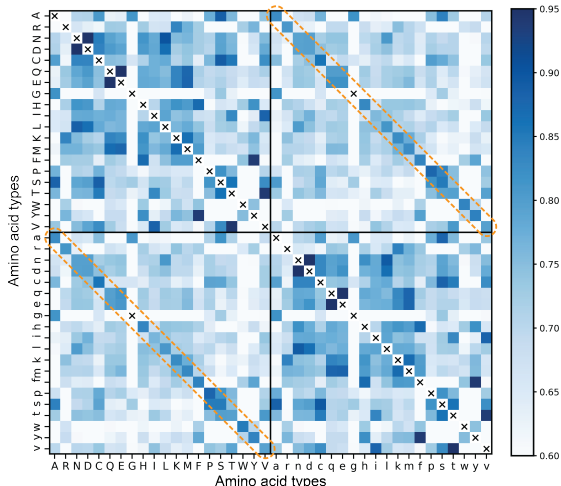


Figure 2. The max-pooled pair-wise Tanimoto shape similarity between L/D amino acids. The similarities between an amino acid and its enantiomer are among the highest compared with similarities between different amino acids. Because similarities between the same amino acid or between "D-Gly" and "L-Gly" are 1.0 by definition, we excluded these entries in the heatmap.

Diffusion stability We establish a continuity theorem on conditional diffusion model. The conditional generation in latent space is an (reversed) SDE sampler:

$$dZ_t = b_\theta(Z_t, t, c) dt + \sigma(t) dW_t, \quad t \in [0, T], \quad (16)$$

where c is the encoded code as the condition of diffusion, b_θ is the learned drift, and W_t is Brownian motion. Let $\mu_c := \mathcal{L}(Z_0 | c)$ denote the output distribution at time $t = 0$. We give a Lipschitz assumption on neural networks,

Assumption 3.3 (Lipschitz drift in state and condition). There exist $L_z, L_c > 0$ such that for all z, z', c, c', t ,

$$\|b_\theta(z, t, c) - b_\theta(z', t, c)\| \leq L_z \|z - z'\|, \quad (17)$$

$$\|b_\theta(z, t, c) - b_\theta(z, t, c')\| \leq L_c \|c - c'\|. \quad (18)$$

Under assumption 3.3, using standard coupling method (Levin & Peres, 2017), we can prove (in Appendix B.4)

Theorem 3.4 (Conditional diffusion is stable in W_2). *Under Assumption 3.3, the solutions of diffusion are close in Wasserstein metric,*

$$W_2(\mu_c, \mu_{c'}) \leq K_{\text{diff}} \|c - c'\|. \quad (19)$$

where K_{diff} is a positive constant.

It follows that under spatial inversion, the target will give similar latent codes of binders to the decoder. We can expect that this leads to the generalization that the axial-sensitive model could almost always generate L binder given D target even no such pairs in the training data.

3.5. Implementation of axial feature injection for D-peptide binder design

Encouraged by the above analysis, we set up to implement AFI within the UniMoMo framework (Kong et al., 2025b), a latent diffusion (Rombach et al., 2022) model that involves a VAE (variational auto-encoder, (Kingma & Welling, 2013)) module and a diffusion module. Briefly, the encoder first maps the input protein structure into a latent code, which is then used to condition the diffusion model. The diffusion generates the latent code of binder, which is decoded into the desired binder using the decoder.

These modules use EPT (Equivariant Pretrained Transformer (Jiao et al., 2024)) as the backbone, which is designed to be $E(3)$ -equivariant. EPT then stacks L layers of self-attention and GVP-FFNs (Jing et al., 2020) that preserve the $E(3)$ -invariance of H and $E(3)$ -equivariance of V . To achieve $SE(3)$ -equivariance, we modify EPT by adding axial vectors to the vector feature V_j' before every FFN layer. We form *axial vector feature* channels based on polar vector features.

Inspired by the representation theory of $SO(3)$, we leverage irreducible decompositions of tensor products to extract geometric features that encode chirality (Thomas et al., 2018; Geiger & Smidt, 2022). While higher-order tensor representations offer finer geometric resolution, they suffer from high computational cost and overfitting to high-frequency noise irrelevant to chirality. We posit that the fundamental parity asymmetry is sufficiently captured by low-order interactions. Therefore, to balance computational efficiency against geometric expressivity, we restrict our framework to decompositions involving up to second-order tensors (see

Appendix B.1). Specifically, we construct three axial vector features:

- (1) the cross product: $u \times v$
- (2) the scalar triple product: $(w \cdot (u \times v)) \cdot w$
- (3) the commutator: $(u \cdot v)(u \times v)$

where $u, v, w \in \mathbb{R}^3$ are adjacent channels of $V' \in \mathbb{R}^{N \times 3 \times K}$. These axial features are then injected via linear mixing of polar and axial channels as shown in Eq. (2). In implementation, we use some normalization on vectors, see Algorithm 1. Finally, we replace $V_j'(X)$ with $\tilde{V}_j(X)$ in every EPT layer to obtain AFI-EPT, as shown in Figure 1. Direct verification shows that (proved in Appendix B.2)

Proposition 3.5. *The constructions of axial vector features above are indeed axial, and the mixed vector features $\tilde{v}_{i,k}(X)$ are $SE(3)$ -equivariant.*

4. Experiment

As discussed above, we implement AFI-EPT based on cross products, triple products, and commutators in the framework of UniMoMo (Kong et al., 2025b). Based on the type of axial vector features, we name these models as PepMirror (cross), PepMirror (triple), and PepMirror (commu.). For ablation, we also train the original UniMoMo with linear peptide data for baseline comparison, which is named UniMoMo (pep.). The published version that trained with three modalities (small molecules, peptides and antibodies) is named UniMoMo (all).

4.1. Latent space analysis

To assess the effect of AFI and provide numerical evidence for our theoretical discussion, we train an autoencoder with AFI-EPT and analyzed the invariant part of the resulting latent codes for amino acids. Specifically, we apply mean pooling over the atom dimension to obtain a fixed-size representation $c(X) \in \mathbb{R}^8$.

Discrepancy To verify Theorem 3.1 and Proposition 3.2, we analyze the latent codes of each pocket structure X in our LNR test set, obtaining $c(X) \in \mathbb{R}^8$. For each sample, we compute the inversion-induced discrepancy $\|c(X) - c(-X)\|_2$ and summarize these distances with box plots (Fig. 3) across samples for several model variants. Introducing AFI consistently increases the L-D discrepancy: the median distance reaches the 10^{-2} scale across different axial-feature constructions, more than four orders of magnitude larger than that without AFI.

Stability and clustering To compare within-type and between-type separations, we estimate mean latent distances for every pair of amino-acid types. Let $\{X_i\}_{i=1}^{20}$ denote

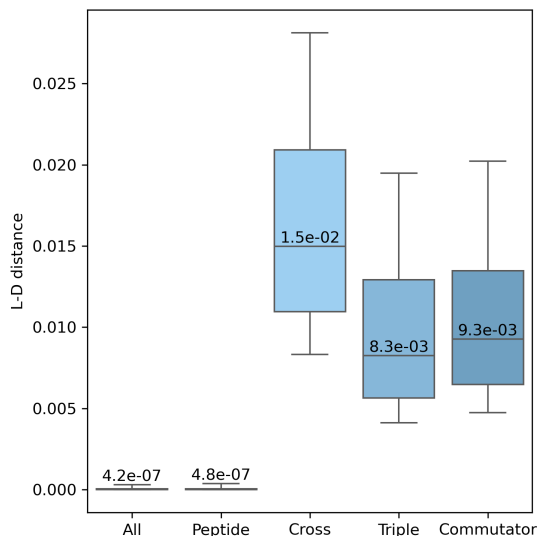


Figure 3. Latent-code distances between each amino acid and its inverted counterpart (X vs. $-X$) for L- and D-forms across different encoder variants. All and Peptide refer to UniMoMo without AFI trained on different datasets (see section 4), and the other three are equipped with AFI based on different axial features. Distances are summarized as box plots over all amino acids. Encoders equipped with AFI exhibit a non-negligible inversion-induced discrepancy. The number on every block is the median distance.

the distributions of the 20 canonical L amino acids, and $\{X_i\}_{i=21}^{40} = \{-X_i\}_{i=1}^{20}$ denote 20 D amino acids. For each $1 \leq i, j \leq 40$, we sample 100 pairs (x_i, x_j) with $x_i \sim X_i$ and $x_j \sim X_j$, and compute

$$\mathbb{E}[\|c(x_i) - c(x_j)\|_2]. \quad (20)$$

We visualize these means as a heatmap (the right panel of Fig. 4). The three diagonals are about two orders of magnitude smaller than the off-diagonal entries, and the t-SNE plot (the left panel of Fig. 4) can further support the tight within-type clustering. For more visualizations, see Appendix A.1.

4.2. In-silico evaluation

4.2.1. BASELINES.

We adopt the following peptide design models as baselines, which can be broadly divided into two categories. The first category assumes L chirality as a built-in prior, including RFDiffusion (Watson et al., 2023), DiffPepBuilder (Wang et al., 2024), PepFlow (Li et al., 2024), D-Flow (Wu et al., 2024), PPFlow (Lin et al., 2024), and PepBridge (Li et al., 2025a). These models treat chirality as a preset constraint rather than a learnable or controllable variable.

The second category does not assume a fixed chirality. PocketXMol (Peng et al., 2025) operates directly on atom coordinates, PepGLAD (Kong et al., 2025a) and UniMoMo (Kong

et al., 2025b) employs coordinate-derived representations without enforcing chiral constraints. However, this flexibility comes at the cost of limited control over chirality consistency, often resulting in mixed-chirality outputs. Notably, PepGLAD utilizes the idealization method after generation, where generated residues are aligned with ideal templates, ensuring L chirality. PepGLAD with idealization is also tested and reported as PepGLAD(ideal).

4.2.2. SETUP AND METRICS

To assess the ability to design D-peptide binders for L-protein targets, we employ large non-redundant complex dataset (LNR) (Tsaban et al., 2022) as our testset. For each model, we input the same binding pocket of either native receptors or the central inverted receptors for L-peptide and D-peptide design, respectively. Generated complexes are then minimized under the Amber14 forcefield (Maier et al., 2015) before the following metrics are calculated:

Chirality. We first assess whether generated peptides exhibit the desired chirality. Specifically, we compute the fraction of residues with the correct chirality, where achiral glycines are excluded. We note that some generated structures suffer with severe clashes, leading to chirality flip during minimization. We therefore calculate the ratio of desired chirality in both raw outputs and minimized structures. For RFDiffusion and PPFlow that only generate backbone atoms, chirality cannot be directly computed. We therefore set the initial chirality and reconstructed $C\beta$ atoms accordingly based on Ramachandran plots (Appendix A.3).

Interface affinity. Because Rosetta energies are statistically derived and exhibit discrepancies between enantiomeric systems (Appendix A.4), we use the score from AutoDock Vina as an alternative metric to assess interface affinity. To evaluate the upper-bound performance of each model, we select the top-1 candidate for each target and report the average binding score. We also compute the proportion of targets for which at least one designed binder achieves a lower interface energy than the native complex, which we report as the interface energy improvement (IMP). To characterize overall performance, we additionally report the mean binding energy across all candidates with negative binding energies. Besides, the ratio of complexes with negative binding energies is reported as the success rate (Suc.).

4.2.3. RESULTS

Chirality. Table 1 reveals two types of behaviours. Frame-based models implicitly enforce L chirality, whereas models without an explicit chirality prior generate mixed-chiral peptides. Notably, PocketXMol, PepGLAD and UniMoMo show $E(3)$ -equivariance: inverting the input structure leads to an accordingly inverted output, which is counterproduc-

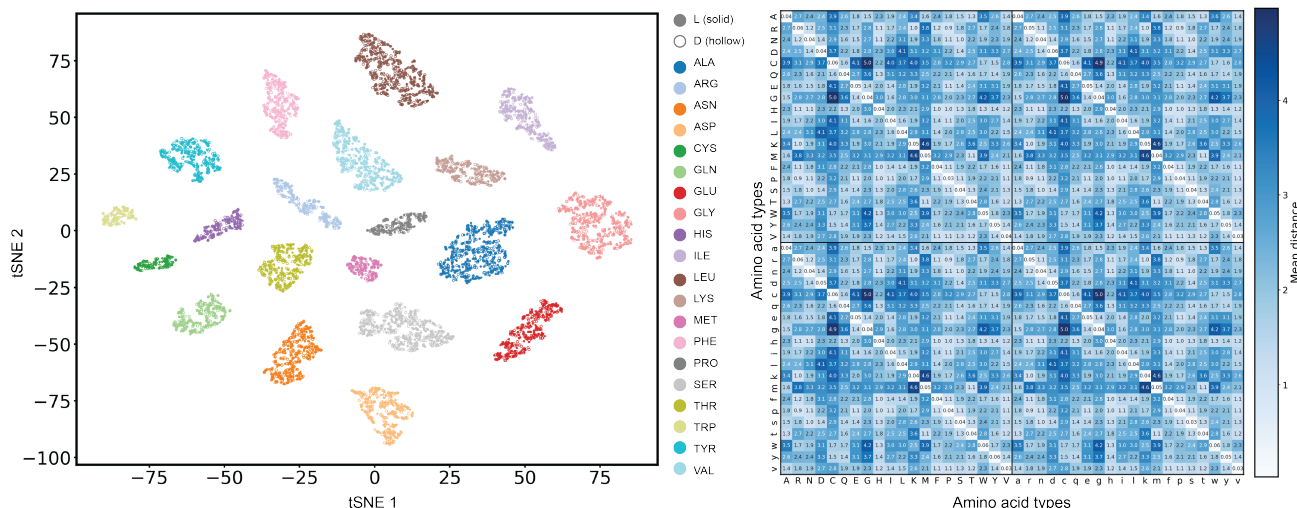


Figure 4. Left: t-SNE of 20 types of amino acids including both L and D chirality. As t-SNE cannot keep distance, we plot the heatmap (right) of mean pairwise latent-code distances among 40 amino-acid classes including 20 L amino acids and 20 D amino acids. The three diagonals are two orders of magnitude smaller than the off-diagonal entries (10^{-2} vs 1), indicating tight within-class clustering and clear inter-class separation. The model we use here is PepMirror (cross), for other models, see Fig. S4, Fig. S5, and Fig. S6

tive for hetero-chiral binder design. This equivariance is reflected by the observation that the L- and D-correct chirality fractions approximately sum to 100%.

After minimization, most structures preserve their initial chirality. For PepBridge, severe intra-ligand clashes lead to loss of chiral consistency during relaxation. Among baselines, PepMirror achieves the highest chirality consistency, and also designs reasonable backbone Ramachadran torsions (Figure S7), suggesting that AFI effectively yields an $SE(3)$ -equivariant mapping that supports hetero-chiral binder design.

Interface affinity. To align with downstream applications where D-peptides are valued for their consistent D-chirality and thus guaranteed stability, we exclude methods that cannot reliably generate peptides with consistent residue-level chirality from the following evaluations.

Among the remaining baselines, RFDiffusion shows a pronounced performance cliff from L- to D-peptide design: the average affinity decreases from -3.30 to -1.77, and IMP drops from 44.09% to 16.13%. Other methods exhibit a similar L–D gap, most clearly in success rate (Table 2). Together with the substantially higher structural diversity observed on D-peptide tasks (Table S3), these results suggest that many models explore a broader yet less target-aligned conformational space for D-peptide design.

PepMirror achieves the strongest overall performance, which is insensitive to the choice of axial vector. It also exhibits the smallest L-to-D degradation, yielding a larger relative advantage on D-peptide tasks. Besides Vina score, we also assess interface quality using Rosetta ddG, while

Table 1. Chirality and minimization backbone-RMSD of models on L/D-peptide design tasks. The best and second best data is labeled orange/light orange for L tasks, and blue/light blue for D tasks.

Models	Task	Right Chirality%	
		Raw	Minimized
RFDiffusion	L	100.0	99.57
	D	100.0	99.15
PPFlow	L	100.0	95.90
	D	100.0	96.31
DiffPepBuilder	L	100.0	98.04
	D	100.0	97.91
PepFlow	L	100.0	99.06
	D	100.0	98.99
D-Flow	L	100.0	98.43
	D	100.0	98.54
Pepbridge	L	100.0	60.04
	D	100.0	60.39
PepGLAD(ideal)	L	100.0	99.00
	D	100.0	99.04
PocketXMol	L	57.83	57.83
	D	43.12	43.12
PepGLAD	L	50.10	50.28
	D	49.94	49.85
UniMoMo(pep.)	L	77.03	76.98
	D	23.90	23.95
UniMoMo(all)	L	84.78	84.70
	D	15.70	15.76
PepMirror(cross)	L	99.93	99.83
	D	99.91	99.81
PepMirror(triple)	L	99.86	99.75
	D	99.84	99.75
PepMirror(commu.)	L	99.95	99.88
	D	99.94	99.88

we note its inconsistency on protein enantiomers. Under this metric, PepMirror remains the top performer and shows a larger advantage among baselines, further supporting its ability to design high-quality hetero-chiral interfaces (Appendix A.4 and Table S5).

4.3. Wet-lab validation

Motivated by PepMirror’s clear advantages in *in-silico* evaluations, we next assess its practical utility for *de novo* D-peptide binder discovery. Using PepMirror (cross), we generate 5,000 D-peptide candidates against CD38 (Cluster of Differentiation 38), a validated therapeutic target in multiple myeloma and an emerging target in NAD⁺-linked immunometabolic disorders. After physics-based and geometry-based filtering (Appendix C.6), we prioritize 12 candidates for chemical synthesis and binding assays. Among them, a 10-mer peptide (D-1412; sequence “trikhytce”) achieve a dissociation constant $K_D \approx 10 \mu\text{M}$, with kinetic and steady-state fittings yielding consistent estimates. Structural inspection of D-1412 suggests multiple sidechain-mediated interactions that depends on correct stereochemistry, supporting PepMirror’s capability to design plausible hetero-chiral interactions (Figure 5). Overall, these results imply a competitive experimental hit rate and further demonstrate the practical utility of PepMirror for mirror-image drug discovery.

Table 2. Interface quality of generated L/D-peptides by different models. The best and second best data is labeled orange/light orange for L tasks, and blue/light blue for D tasks.

Models	Task	Suc.%	Avg.	Top	IMP%
RFDiffusion	L	99.52	-3.30	-5.14	44.09
	D	98.58	-1.77	-3.78	16.13
DiffPepBuilder	L	86.56	-3.58	-5.44	56.99
	D	80.14	-3.38	-5.23	50.54
PepFlow	L	99.41	-3.31	-4.36	13.98
	D	96.78	-2.75	-4.15	16.13
D-Flow	L	99.31	-3.33	-4.41	10.75
	D	97.52	-3.11	-4.54	22.58
PPFlow	L	65.94	-2.58	-5.09	40.86
	D	64.46	-2.64	-5.21	48.39
PepGLAD(ideal)	L	94.56	-3.27	-5.10	40.86
	D	95.08	-3.26	-5.11	43.01
PepMirror(cross)	L	99.67	-4.27	-5.81	69.89
	D	99.76	-4.15	-5.69	63.44
PepMirror(triple)	L	99.73	-4.31	-5.88	69.89
	D	99.72	-4.20	-5.75	67.74
PepMirror(commu.)	L	99.73	-4.34	-5.89	76.34
	D	99.75	-4.25	-5.87	72.04

5. Conclusion and Discussion

In this work, we propose AFI-EPT that injects axial vector features into polar vector features in EPT (Jiao et al.,

2024). By implementing this module in latent diffusion framework, we build PepMirror that design mirror-image peptide binders for native protein targets. Through theoretical analysis and experiments, we show that the latent codes of L and D amino acids will have close but different representations, so that the model acquires the ability to distinguish different chirality while maintains the ability to generate reasonable structures given unseen D-targets as input. The evaluation results show that PepMirror have advanced performance compared with existing peptide binder design models. On top of this, we tested PepMirror in a real-world D-peptide binder design campaign, and successfully identified a D-binder against CD38 with a KD of 10 μM out of 12 designs.

Although PepMirror has achieved best-in-class performance and, for the first time, demonstrate utility in wet-lab experiments, we recognize that opportunities remain for further exploration. First, our theoretical analysis of AFI focuses on the feature-mixing mechanism under simplifying assumptions, rather than providing an end-to-end theory of the trained network (including optimization and generalization). A more complete account of how axial information propagates through subsequent equivariant blocks remains an open direction. Besides, we evaluate three axial-feature constructions, but many others are possible. Systematically designing axial features that yield the best empirical performance is an interesting problem for future work.

Nonetheless, our work shows the feasibility of designing wet-lab validated mirror-image peptide binders with generative AI for the first time, which not only provides a useful tool, but also inspires new insights in handling chirality in protein design.

Impact Statement

This paper presents work whose goal is to advance the field of machine learning based functional protein design. There are many potential societal consequences of our work, none of which we feel must be specifically highlighted here.

References

- Adams, K., Pattanaik, L., and Coley, C. W. Learning 3d representations of molecular chirality with invariance to bond rotations. *arXiv preprint arXiv:2110.04383*, 2021.
- Blackmond, D. G. The origin of biological homochirality. *Cold Spring Harbor perspectives in biology*, 2(5): a002147, 2010.
- Cao, L., Coventry, B., Goresnik, I., Huang, B., Sheffler, W., Park, J. S., Jude, K. M., Marković, I., Kadam, R. U., Verschueren, K. H., et al. Design of protein-binding

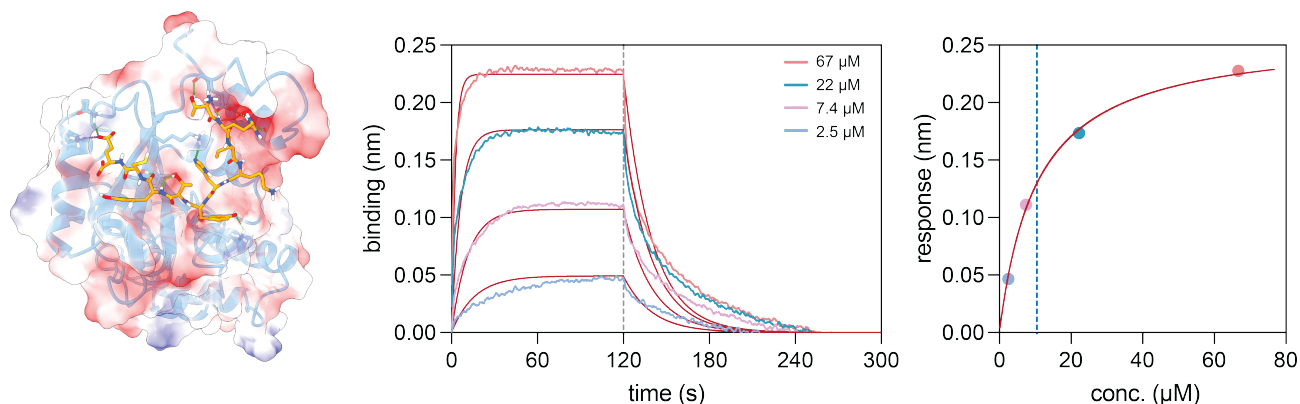


Figure 5. The identified D-peptide binder against CD38. Left: Complex structure of D-1412 and CD38 generated by PepMirror (cross), where multiple interactions can be identified. Middle: Stacked curves of association and dissociation under different concentrations with kinetic fitting. Right: Steady state fitting of the max response for each concentration, the blue line is the observed KD.

- proteins from the target structure alone. *Nature*, 605 (7910):551–560, 2022.
- Chang, H.-N., Liu, B.-Y., Qi, Y.-K., Zhou, Y., Chen, Y.-P., Pan, K.-M., Li, W.-W., Zhou, X.-M., Ma, W.-W., Fu, C.-Y., et al. Blocking of the pd-1/pd-11 interaction by ad-peptide antagonist for cancer immunotherapy. *Angewandte Chemie International Edition*, 54(40):11760–11764, 2015.
- Coors, B., Condurache, A. P., and Geiger, A. Spherenet: Learning spherical representations for detection and classification in omnidirectional images. In *Proceedings of the European conference on computer vision (ECCV)*, pp. 518–533, 2018.
- Du, Y., Chen, J., and Schwaller, P. Pretrained graph transformers for chirality-related tasks. In *AI for Accelerated Materials Design-Vienna*, 2024.
- Engel, H., Guischart, F., Krause, F., Nandy, J., Kaas, P., Hoefflin, N., Koehn, M., Kilb, N., Voigt, K., Wolf, S., et al. findr: A web server for in silico d-peptide ligand identification. *Synthetic and Systems Biotechnology*, 6(4): 402–413, 2021.
- Foster, M. S. Rotations in 3d, $\mathfrak{so}(3)$, and $\mathfrak{su}(2)$, version 2.1. Lecture notes, Rice University, 2021.
- Fuchs, F., Worrall, D., Fischer, V., and Welling, M. SE(3)-Transformers: 3D Roto-Translation Equivariant Attention Networks. In *Advances in Neural Information Processing Systems*, volume 33, pp. 1970–1981. Curran Associates, Inc., 2020.
- Fulton, W. and Harris, J. *Representation Theory*, volume 129 of *Graduate Texts in Mathematics*. Springer New York, New York, NY, 2004. ISBN 978-3-540-00539-1 978-1-4612-0979-9.
- Gaiński, P., Koziarski, M., Tabor, J., and Śmieja, M. Chien: Embracing molecular chirality with graph neural networks. In *Joint European Conference on Machine Learning and Knowledge Discovery in Databases*, pp. 36–52. Springer, 2023.
- Garton, M., Nim, S., Stone, T. A., Wang, K. E., Deber, C. M., and Kim, P. M. Method to generate highly stable d-amino acid analogs of bioactive helical peptides using a mirror image of the entire pdb. *Proceedings of the National Academy of Sciences*, 115(7):1505–1510, 2018.
- Geiger, M. and Smidt, T. E3nn: Euclidean Neural Networks, 2022.
- Hall, B. C. *Lie Groups, Lie Algebras, and Representations: An Elementary Introduction*, volume 222 of *Graduate Texts in Mathematics*. Springer International Publishing, Cham, 2015. ISBN 978-3-319-13466-6 978-3-319-13467-3.
- Han, J., Cen, J., Wu, L., Li, Z., Kong, X., Jiao, R., Yu, Z., Xu, T., Wu, F., Wang, Z., et al. A survey of geometric graph neural networks: Data structures, models and applications. *Frontiers of Computer Science*, 19(11):1911375, 2025.
- Jackson, J. *Classical Electrodynamics*. Wiley, 2021. ISBN 978-1-119-77076-3.
- Jiao, R., Kong, X., Yu, Z., Huang, W., and Liu, Y. Equivariant pretrained transformer for unified geometric learning on multi-domain 3d molecules. In *ICLR 2024 Workshop on Generative and Experimental Perspectives for Biomolecular Design*, 2024.
- Jing, B., Eismann, S., Suriana, P., Townshend, R. J., and Dror, R. Learning from protein structure with geometric

-
- vector perceptrons. *arXiv preprint arXiv:2009.01411*, 2020.
- Jumper, J., Evans, R., Pritzel, A., et al. Highly accurate protein structure prediction with AlphaFold. *Nature*, 596: 583–589, 2021.
- Kingma, D. P. and Welling, M. Auto-encoding variational bayes. *arXiv preprint arXiv:1312.6114*, 2013.
- Kirchmeyer, M., Pinheiro, P. O., Willett, E., Martinkus, K., Kleinhenz, J., Makowski, E., Watkins, A., Gligorijevic, V., Bonneau, R., and Saremi, S. Unified all-atom molecule generation with neural fields. In *The 39th Annual Conference on Neural Information Processing Systems*, 2025.
- Kong, X., Jia, Y., Huang, W., and Liu, Y. Full-atom peptide design with geometric latent diffusion. *Advances in Neural Information Processing Systems*, 37:74808–74839, 2025a.
- Kong, X., Zhang, Z., Zhang, Z., Jiao, R., Ma, J., Huang, W., Liu, K., and Liu, Y. Unimomo: Unified generative modeling of 3d molecules for de novo binder design. In *The 42nd International Conference on Machine Learning*, 2025b.
- Kremsmayr, T., Aljnabi, A., Blanco-Canosa, J. B., Tran, H. N., Emidio, N. B., and Muttenthaler, M. On the utility of chemical strategies to improve peptide gut stability. *Journal of medicinal chemistry*, 65(8):6191–6206, 2022.
- Lander, A. J., Jin, Y., and Luk, L. Y. D-peptide and d-protein technology: recent advances, challenges, and opportunities. *ChemBioChem*, 24(4):e202200537, 2023.
- Levin, D. A. and Peres, Y. *Markov chains and mixing times*, volume 107. American Mathematical Soc., 2017.
- Li, G., Zhao, X., Wu, F., and Laue, S. Joint design of protein surface and backbone using a diffusion bridge model. In *The 39th Annual Conference on Neural Information Processing Systems*, 2025a.
- Li, J., Cheng, C., Wu, Z., Guo, R., Luo, S., Ren, Z., Peng, J., and Ma, J. Full-atom peptide design based on multimodal flow matching. In *Proceedings of the 41st International Conference on Machine Learning (ICML 2024)*, pp. 27615–27640, 2024.
- Li, Y., Huang, L., Ding, Z., Wei, X., Wang, C., Yang, H., Wang, Z., Liu, C., Shi, Y., Jin, P., Qin, T., Gerstein, M., and Zhang, J. E2Former: An Efficient and Equivariant Transformer with Linear-Scaling Tensor Products. In *The Thirty-ninth Annual Conference on Neural Information Processing Systems*, 2025b.
- Lin, H., Zhang, O., Zhao, H., Jiang, D., Wu, L., Liu, Z., Huang, Y., and Li, S. Z. PPFlow: target-aware peptide design with torsional flow matching. In *Proceedings of the 41st International Conference on Machine Learning*, pp. 30510–30528, 2024.
- Maier, J. A., Martinez, C., Kasavajhala, K., Wickstrom, L., Hauser, K. E., and Simmerling, C. ff14sb: improving the accuracy of protein side chain and backbone parameters from ff99sb. *Journal of chemical theory and computation*, 11(8):3696–3713, 2015.
- Morehead, A. and Cheng, J. Geometry-complete perceptron networks for 3d molecular graphs. *Bioinformatics*, 40(2): btae087, 2024.
- Notin, P., Rollins, N. J., Gal, Y., Sander, C., and Marks, D. Machine learning for functional protein design. *Nature Biotechnology*, 42:216–228, 2024.
- Pasteur, L. Memoires sur la relation qui peut exister entre la forme cristalline et al composition chimique, et sur la cause de la polarization rotatoire. *Compt. rend.*, 26: 535–538, 1848.
- Peng, X., Guo, F., Guo, R., Sun, J., Guan, J., Jia, Y., Xu, Y., Huang, Y., Zhang, M., Peng, J., Wang, X., Han, C., Wang, Z., and Ma, J. Atom-level generative foundation model for molecular interaction with pockets. *bioRxiv*, 2025. bioRxiv:2024.10.17.618827.
- Qi, Y.-K., Zheng, J.-S., and Liu, L. Mirror-image protein and peptide drug discovery through mirror-image phage display. *Chem*, 10(8):2390–2407, 2024.
- Rombach, R., Blattmann, A., Lorenz, D., Esser, P., and Ommer, B. High-resolution image synthesis with latent diffusion models. In *Proceedings of the IEEE/CVF conference on computer vision and pattern recognition*, pp. 10684–10695, 2022.
- Satorras, V. G., Hoogeboom, E., and Welling, M. E(n) Equivariant Graph Neural Networks, 2022.
- Schneider, N., Lewis, R. A., Fechner, N., and Ertl, P. Chiral cliffs: Investigating the influence of chirality on binding affinity. *ChemMedChem*, 13(13):1315–1324, 2018.
- Smidt, T. E., Geiger, M., and Miller, B. K. Finding symmetry breaking order parameters with Euclidean neural networks. *Physical Review Research*, 3(1):L012002, 2021.
- Sun, K., Li, S., Zheng, B., Zhu, Y., Wang, T., Liang, M., Yao, Y., Zhang, K., Zhang, J., Li, H., et al. Accurate de novo design of heterochiral protein–protein interactions. *Cell Research*, 34(12):846–858, 2024.

-
- Thomas, N., Smidt, T., Kearnes, S., Yang, L., Li, L., Kohlhoff, K., and Riley, P. Tensor field networks: Rotation- and translation-equivariant neural networks for 3D point clouds, 2018.
- Tsaban, T., Varga, J. K., Avraham, O., Ben-Aharon, Z., Khramushin, A., and Schueler-Furman, O. Harnessing protein folding neural networks for peptide–protein docking. *Nature communications*, 13(1):176, 2022.
- Vershynin, R. *High-Dimensional Probability: An Introduction with Applications in Data Science*. Cambridge University Press, 2018. ISBN 978-1-108-41519-4.
- Wang, F., Wang, Y., Feng, L., Zhang, C., and Lai, L. Target-specific de novo peptide binder design with DiffPep-Builder. *Journal of Chemical Information and Modeling*, 64(24):9135–9149, 2024.
- Watson, J. L., Juergens, D., Bennett, N. R., et al. De novo design of protein structure and function with RFdiffusion. *Nature*, 620:1089–1100, 2023.
- Wedig, S., Elijošius, R., Schran, C., and Schaaf, L. L. Rem3di: Learning smooth, chiral 3d molecular representations from equivariant atomistic foundation models. In *NeurIPS 2025 Workshop on Symmetry and Geometry in Neural Representations*, 2025.
- Wu, F., Jin, S., Tang, X., Xu, J., Gerstein, M., and Zou, J. D-Flow: Multi-modality flow matching for D-peptide design. *arXiv preprint arXiv:2411.10618*, 2024.
- Zhou, X., Zuo, C., Li, W., Shi, W., Zhou, X., Wang, H., Chen, S., Du, J., Chen, G., Zhai, W., et al. A novel d-peptide identified by mirror-image phage display blocks tigit/pvr for cancer immunotherapy. *Angewandte Chemie International Edition*, 59(35):15114–15118, 2020.

A. Additional Results and Discussion

A.1. Latent space analysis

We summarize the PCA, t-SNE, and UMAP visualizations, together with the pairwise distance heatmaps, for the three axial features used in AFI-EPT. Figures S1, S4, S5, and S6 show that all three features organize amino-acid embeddings into 20 well-separated clusters in latent space, corresponding to the 20 canonical residue types, with L/D isomers of the same residue co-clustering. The distance heatmaps across residue types further corroborate this 20-cluster structure. The parameters and explained variance ratios are listed in Table S1 and Table S2.

We also show the zoom-in version of the tSNE latent clusters in Figure S2 and S3, where the latent codes of L/D chirality for each amino acid type are plotted separately.

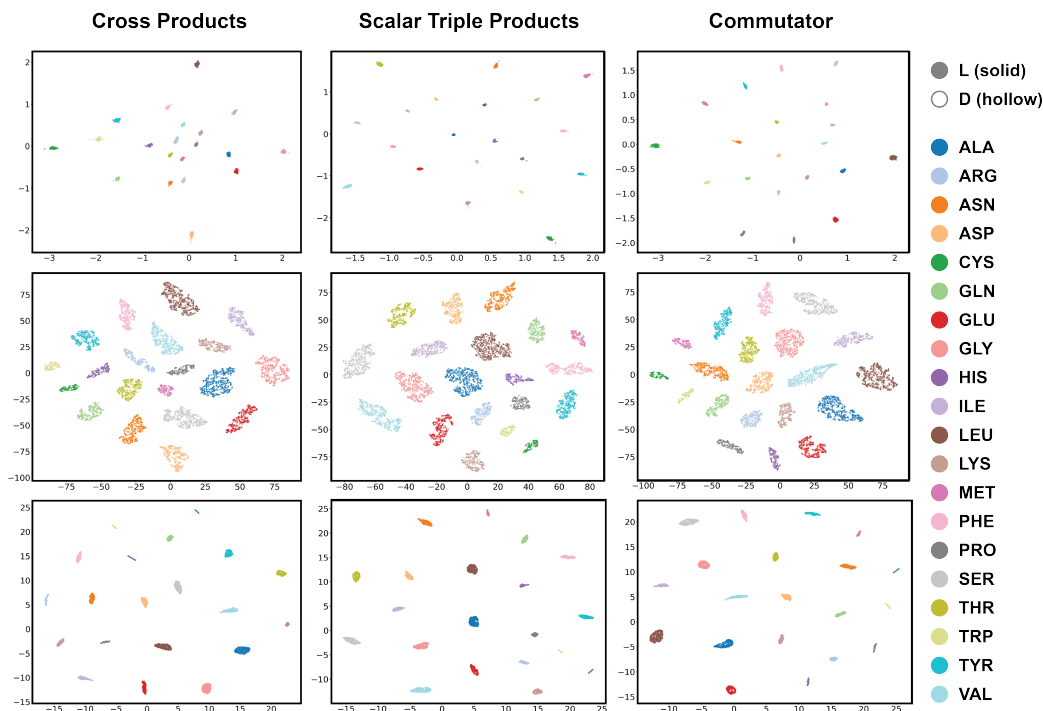


Figure S1. visualization of the clustering results of the LNR latent codes generated from PepMirror. From top to bottom, the rows display the clustering results using PCA, t-SNE, and UMAP, respectively.

Table S1. Parameters used in latent clustering

Method	Parameter	Value
PCA	random state	12
	perplexity	50.0
tSNE	random state	12
	metric	euclidean
UMAP	n neighbors	75
	random state	12
	min dist	0

Table S2. Explained variance ratios in PCA

Cross		Triple		Commutator	
PC	ratio	PC	ratio	PC	ratio
1	0.346	1	0.523	1	0.547
2	0.342	2	0.477	2	0.453
3	0.312	3	3.4e-5	3	2.5e-5
4	4.9e-5	4	2.2e-5	4	2.1e-5
5	1.7e-5	5	9.9e-6	5	1.2e-5
6	1.2e-5	6	8.0e-6	6	6.9e-6
7	6.8e-6	7	7.3e-6	7	4.3e-6
8	4.1e-6	8	5.3e-6	8	2.7e-6

A.2. Evaluations on native interface coverage and diversity

Settings For native interface recovery. Although D-peptide binders are not expected to match native binder sequences, native complexes provide a useful reference for plausible binding poses. We computed binding site recovery (BSR) to

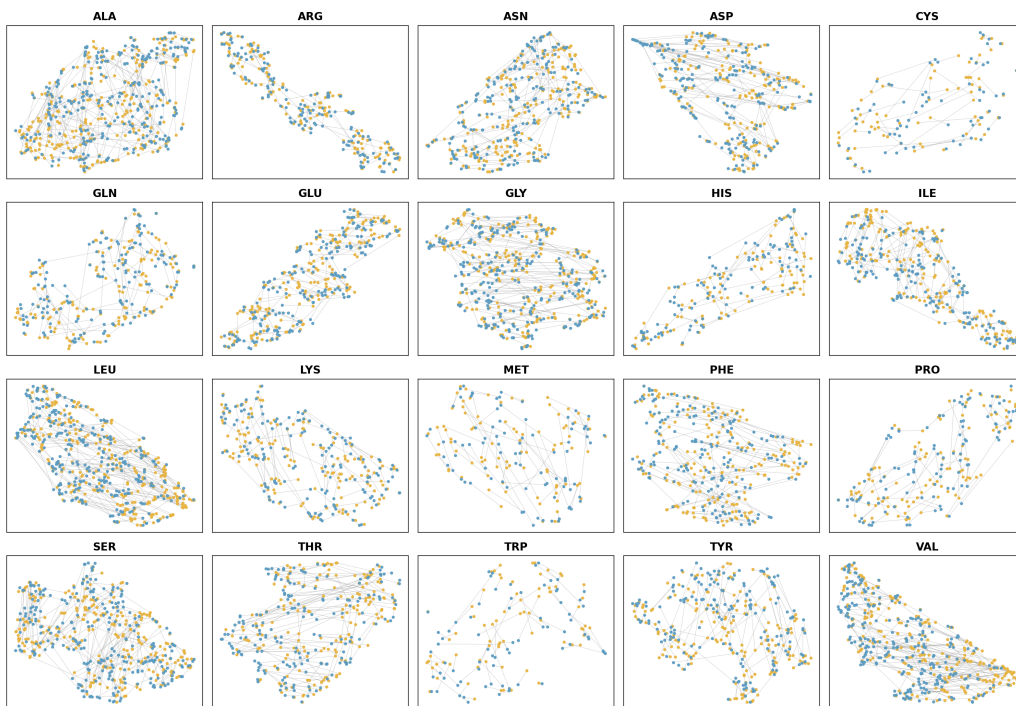


Figure S2. Visualization of the tSNE clustering results of the LNR latent codes generated from PepMirror(cross). Latent codes for L amino acids are orange, latent codes for D amino acids are blue, and a residue and its inverted structure are connected with a gray line.

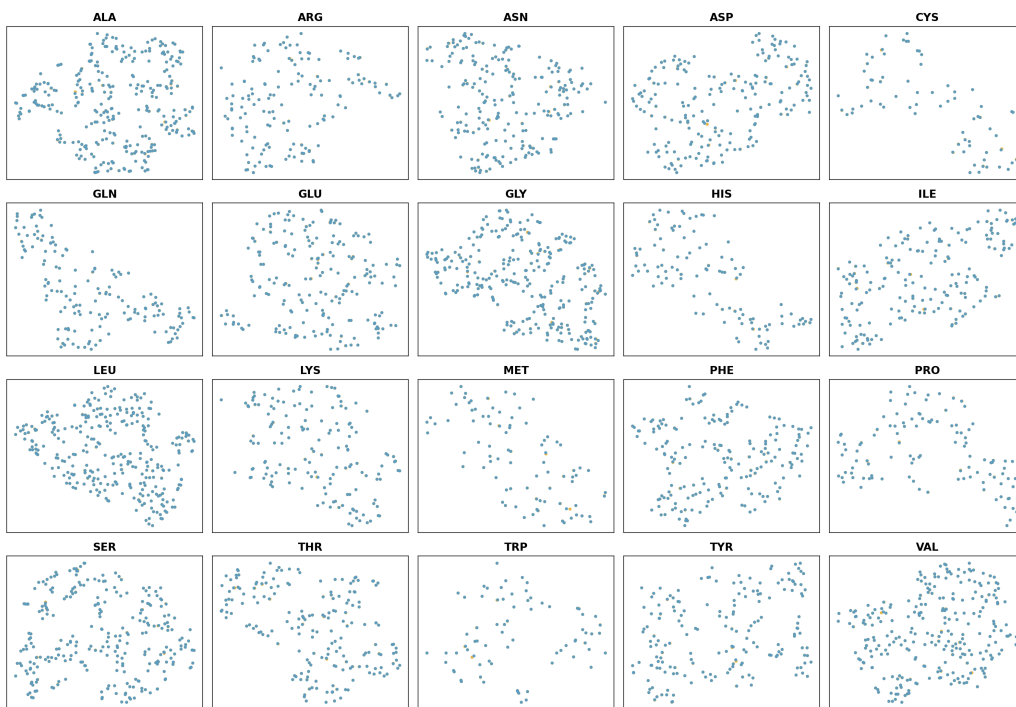


Figure S3. Visualization of the tSNE clustering results of the LNR latent codes generated from UniMoMo(pep.). Latent codes for L amino acids are orange, latent codes for D amino acids are blue, and a residue and its inverted structure are connected with a gray line.

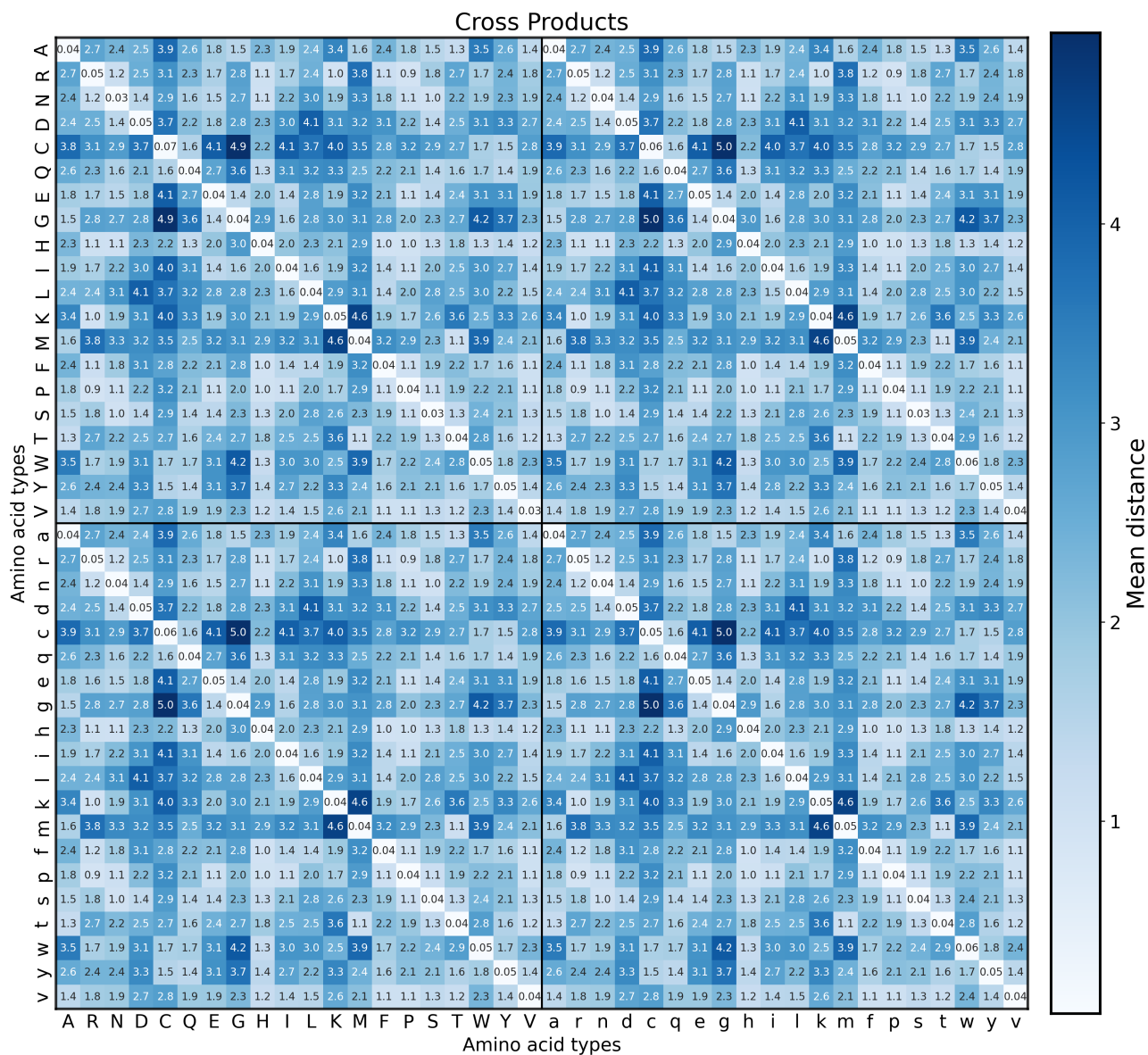


Figure S4. Heatmaps of mean-pooled euclidean distances between each amino acid type pair. The encoder of PepMirror(cross) is employed for encoding.

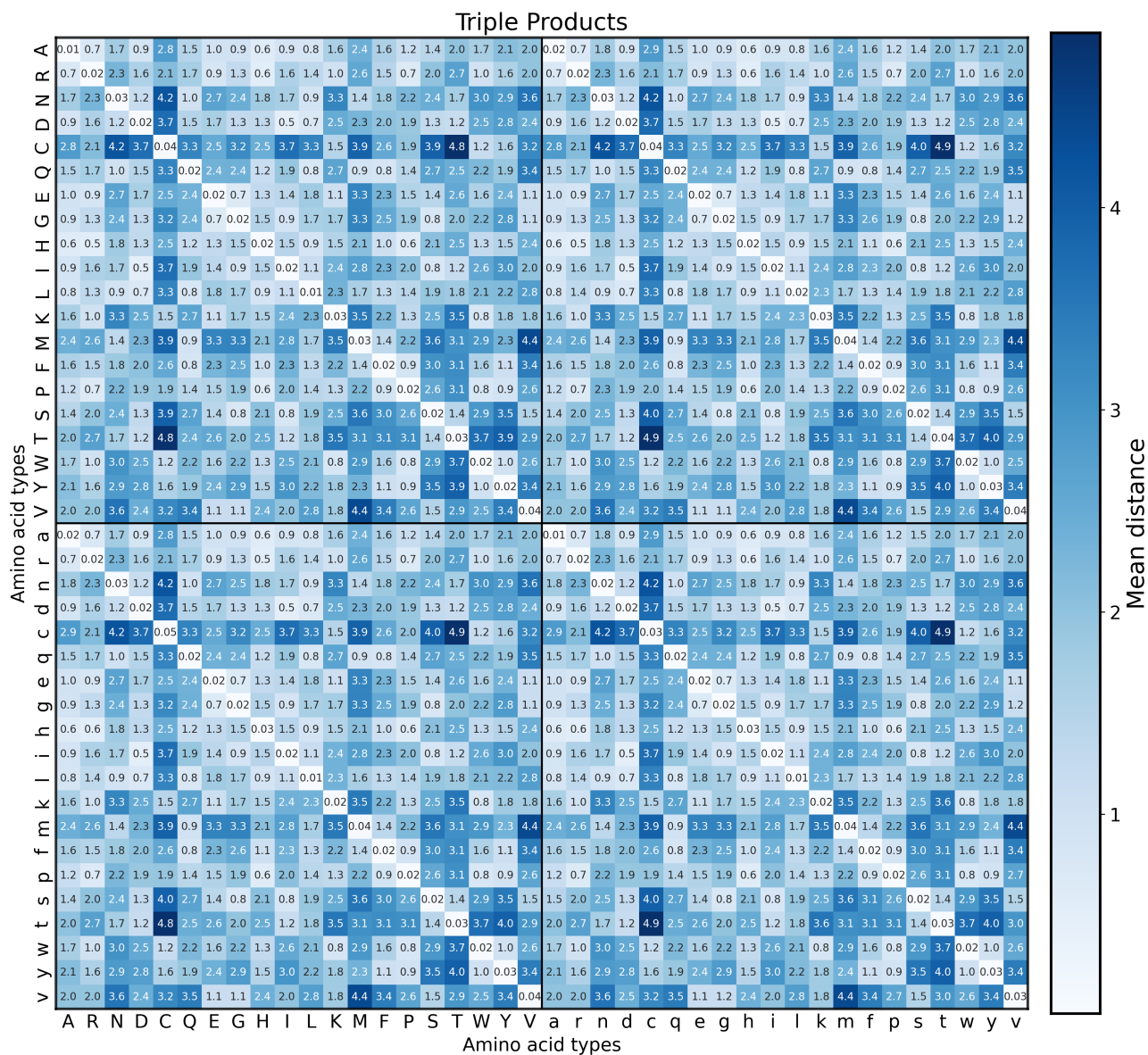


Figure S5. Heatmaps of mean-pooled euclidean distances between each amino acid type pair. The encoder of PepMirror(triple) is employed for encoding.

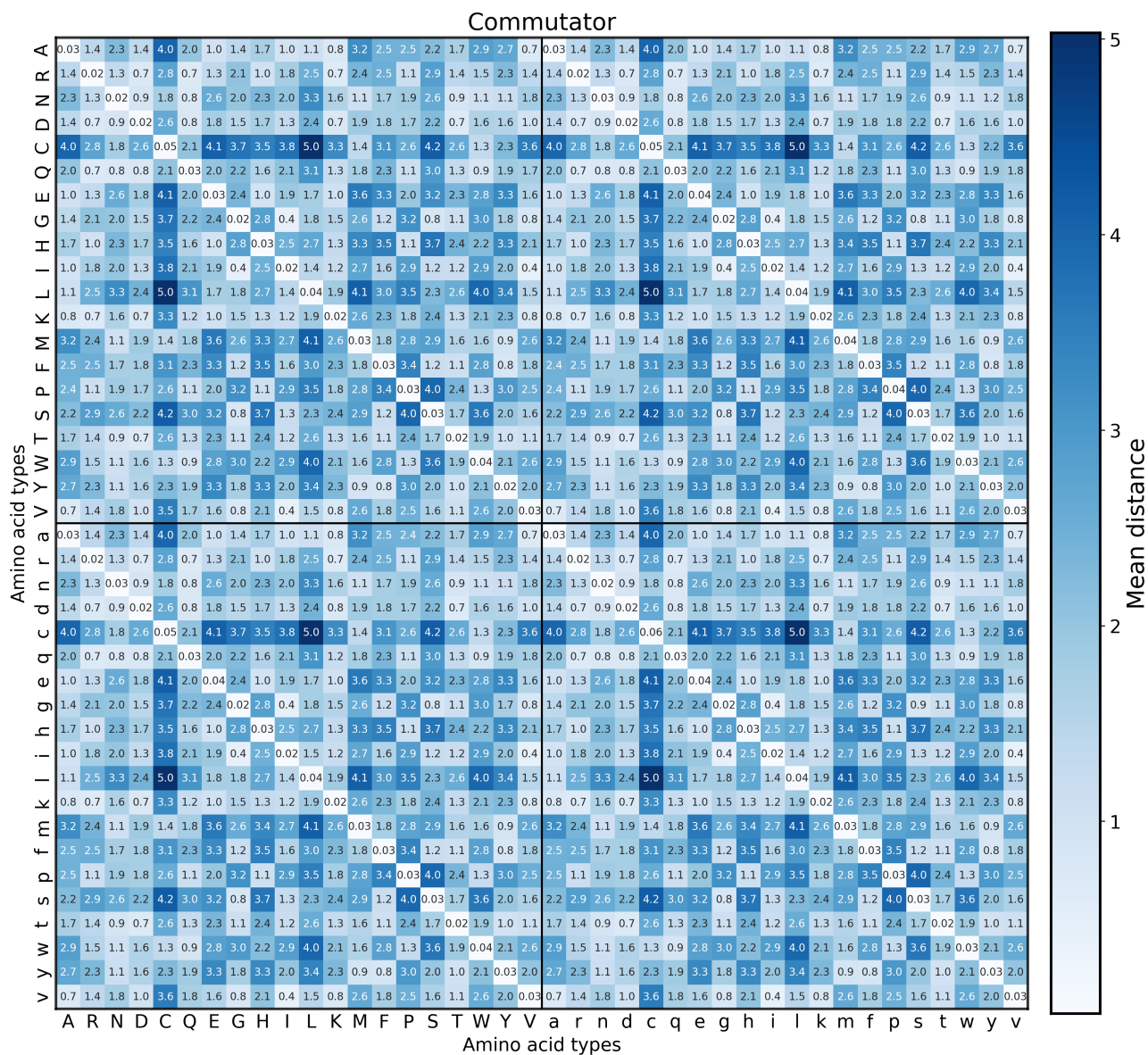


Figure S6. Heatmaps of mean-pooled euclidean distances between each amino acid type pair. The encoder of PepMirror(commutator) is employed for encoding.

Table S3. Native interface coverage and diversity of generated L/D peptides by different models. The highest and the second highest value of each metric are labeled with orange/light orange for L tasks, and blue/light blue for D tasks.

Models	Task	BSR	Div_{seq}	Div_{struct}
RFDiffusion	L	62.39	0.496	0.701
	D	35.53	0.271	0.934
DiffPepBuilder	L	90.24	0.211	0.319
	D	89.63	0.237	0.383
PepFlow	L	82.33	0.095	0.172
	D	73.57	0.145	0.346
D-Flow	L	81.48	0.063	0.355
	D	79.93	0.082	0.446
PPFlow	L	82.01	0.856	0.916
	D	81.78	0.859	0.920
PepGLAD(ideal)	L	78.05	0.860	0.868
	D	78.24	0.861	0.867
PepMirror(cross)	L	87.51	0.846	0.719
	D	86.64	0.847	0.717
PepMirror(triple)	L	87.19	0.840	0.682
	D	86.52	0.848	0.727
PepMirror(commu.)	L	88.12	0.839	0.648
	D	87.34	0.848	0.686

quantify how well the designed interface overlaps with the native binding site, capturing both the contact coverage and the epitope precision. **For diversity.** Generating diverse candidates provides more starting points for downstream optimization. We quantified diversity at both the sequence and structure levels by clustering generated peptides using sequence overlap and $C\alpha$ RMSD thresholds, respectively. Diversity is defined as $N_{clusters}/N_{samples}$, reported as Div_{Seq} and Div_{Struct} .

Results and analysis Interface recovery and diversity pull the design in different directions, reflecting the trade-off between fidelity to the native binding mode and exploration for alternative conformations that could be better solutions. Therefore, although these metrics are often treated as “the higher, the better”, excessively large values in either can be undesirable in practice. Overly high recovery may indicate limited exploration, whereas overly high diversity can signal weak adherence to the specified binding mode.

For most models, generated peptides cover more than 50% of the native epitope, with DiffPepBuilder showing the highest coverage at around 90%. This proximity to native states likely contributes to the competitive average and top interface energy in Table 2, where DiffPepBuilder nearly matches PepMirror. However, such adherence restricts sequence and structural diversity, leading to a markedly lower IMP than PepMirror despite similar affinity.

In contrast, RFDiffusion shows substantially lower coverage, especially on D-peptide design tasks. Consistently, it exhibits high D-peptide structural diversity (0.934), which largely stems from limited site specificity: many designs drift from the designated hotspots rather than diversifying within the intended pocket. PPFlow shows high diversity in both sequence and structure, likely due to weaker pocket-shape conditioning and limited clash control: peptides are less constrained by the intended geometry and often sample a broader, clash-prone conformational space. Unlike RFDiffusion, which frequently drifts away from the target region, PPFlow remains more engaged with the receptor, inducing more complex interfaces and consequently higher sequence diversity.

By comparison, PepMirror maintains BSR and diversity within a reasonable range, with only a small gap between L- and D-peptide tasks. This balance between reliable epitope anchoring and principled exploration may explain its strong IMP (Table 2 and Table S5).

A.3. Ramachandran plot analysis

The backbone conformation of a residue can be characterized by two torsions, known as the Ramachandran angles. Specifically, ϕ is the dihedral angle around the $N-C\alpha$ bond defined by the four atoms $(C_{i-1}, N_i, C_{\alpha i}, C_i)$, and ψ is the dihedral angle around the $C\alpha-C$ bond defined by $(N_i, C_{\alpha i}, C_i, N_{i+1})$. Statistical analyses on known protein structures have shown that there is a preferred area in the joint distribution of (ϕ, ψ) , which depends on side-chain structures. In other words,

Table S4. The energy discrepancy of protein enantiomers calculated by Rosetta

Entry	Backbone		Sidechain		Jump	Round	Score Function	Δ Total Energy	Δ ddG	Δ dG
	Lig.	Rec.	Lig.	Rec.						
1	True	False	True	True	False	2	ref2015	5098.10	19.95	16.61
2	True	True	True	True	False	2	ref2015	2772.00	13.25	12.03
3	True	True	True	True	True	2	ref2015	2747.82	12.27	11.49
4	True	True	True	True	False	5	ref2015	2757.52	13.09	11.81
5	True	True	True	True	False	2	beta_nov16	2469.61	13.34	12.05

allowed conformations concentrate in certain regions of the ϕ - ψ plane. By definition, the Ramachandran distribution of a protein is the central inversion of that of its mirror-image, i.e., $(\phi, \psi) \mapsto (-\phi, -\psi)$. Therefore, Ramachandran plots provide a diagnostic for: (i) the physical plausibility of peptide backbones, and (ii) whether the sampled torsional preferences are consistent with the intended residue chirality.

Figure S7 reports the Ramachandran plots of peptides generated by some models. For RFDiffusion and PPFlow in line 1, we show that the backbone of generated peptides align to be L-residues no matter what chirality the receptor is. In line 2, we show that although idealization could ensure homo L-chirality for PepGLAD, the mainchain torsions are still not ideal for L-peptides. In line 3, we show that UniMoMo(all) with original EPT has the E(3)-equivariant feature, where inverting targets causes the inversion of Ramachandran plots. In contrary, PepMirror with AFI-EPT not only maintains chirality at residue level, but also keeps backbone dihedrals to be suitable for L-peptides.

A.4. Interface affinity analysis by Rosetta

Discrepancy of Rosetta score between protein enantiomers. To compare interface energies between L-L and L-D complexes reliably, the scoring function must be *E(3)-invariant*: a structure and its enantiomer should receive the same total energy, and a complex should have the same binding (interface) energy as its mirror image.

Although Rosetta technically supports D-amino-acid residues, we empirically observe substantial inconsistencies when scoring enantiomeric inputs. Specifically, when we provide complexes from the LNR dataset and their mirror images to Rosetta and compute both total and interface energies, the resulting scores differ markedly. This discrepancy persists across multiple score functions and remains even after varying relaxation protocols, indicating that the lack of enantiomer consistency is not easily mitigated by choices of score functions or relax settings (Table. S4).

A detailed breakdown of the score terms reveals that the discrepancy is dominated by an abnormal increase in `fa_rep` after spatial inversion. We hypothesize that this behavior stems from Rosetta’s discrete, rotamer-library-based sampling. Because statistical coverage for D-protein conformations is limited, conformers that are deemed permissible for L-proteins may become underrepresented for their D counterparts. As a result, the relax trajectory can be biased, leading to higher steric repulsion. In contrast, full-atom forcefield-based tools such as AutoDock Vina yield nearly identical scores for enantiomeric protein complexes (the average score for L and D are both -4.57). We therefore adopt Vina as our interface-affinity evaluation metric. Nonetheless, we still report the results of interface affinity evaluation based on Rosetta for references.

Interface affinity evaluation based on Rosetta.

We follow the evaluation protocol in entry 1 of Table S4 to compute Rosetta ddG. Analogous to the interface affinity metrics in Section 4.2.2, we report (i) top-1 ddG across multiple samples and the corresponding interface energy improvement (IMP) to capture best-case performance, and (ii) the success rate (fraction of designs with $ddG < 0$) and the mean ddG over successful designs to reflect overall quality. For consistency, IMP is referenced to ddG values computed on L-L LNR complexes, while we note that directly comparing D-L to L-L may be biased due to Rosetta’s chirality-dependent discrepancy.

Table S5 exhibits trends consistent with Table 2. In particular, the L-D performance cliff becomes more pronounced under Rosetta ddG. Some baselines achieve performance comparable to PepMirror on L-peptide tasks, yet suffer substantial degradations across metrics on D-peptide tasks. Consequently, PepMirror shows a markedly larger advantage on D-peptide design in this evaluation.

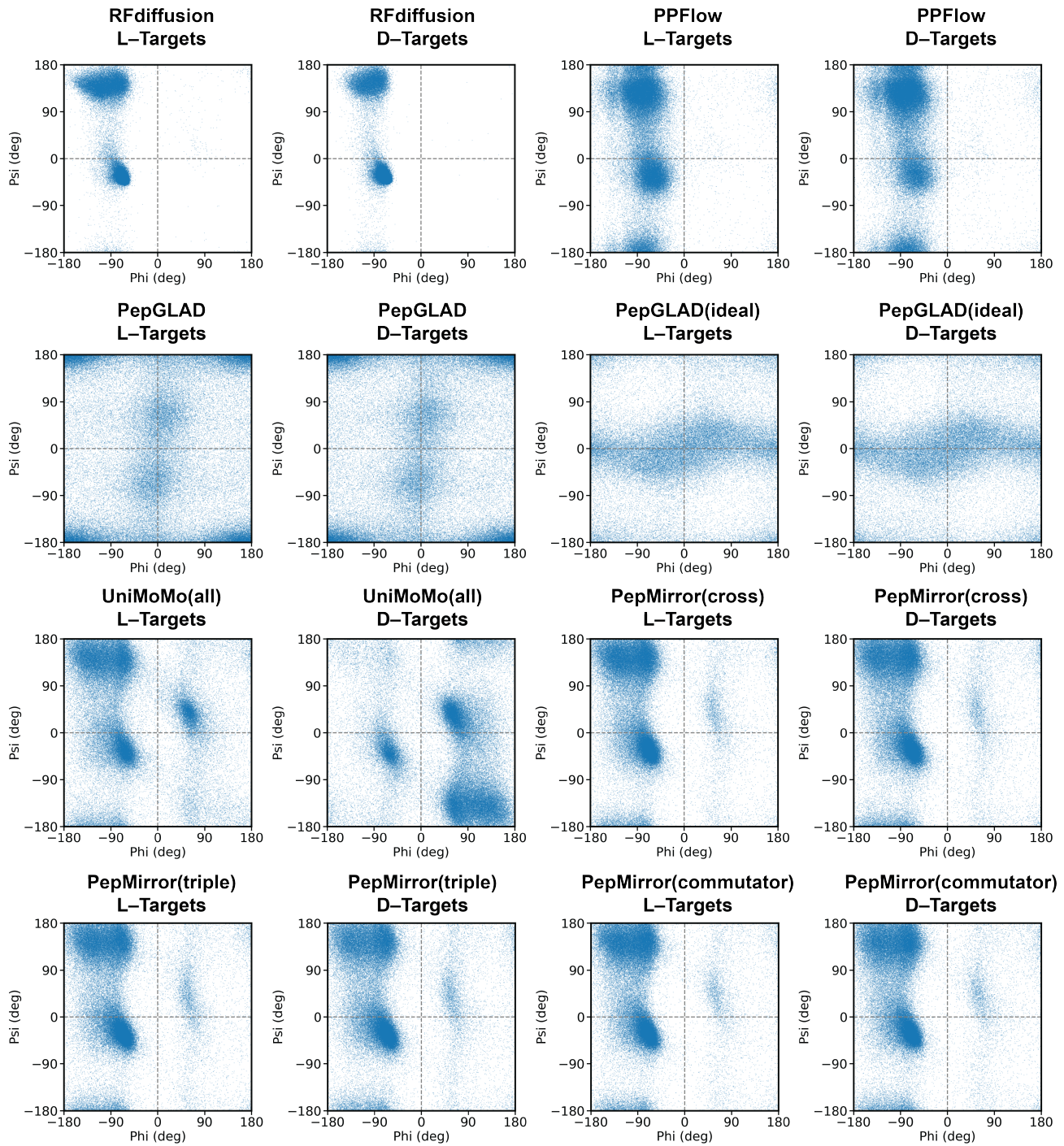


Figure S7. Ramachandran plots of generated peptides from certain models.

Table S5. Interface quality of generated L/D peptides evaluated by Rosetta. The best and second best data is labeled orange/light orange for L tasks, and blue/light blue for D tasks.

Models	Task	Suc.	Avg.	Top	IMP
RFDiffusion	L	71.87	-22.86	-38.87	50.00
	D	49.82	-7.30	-19.09	10.00
DiffPepBuilder	L	51.82	-15.37	-22.58	24.44
	D	31.30	-12.66	-6.66	16.67
PepFlow	L	96.99	-20.45	-33.02	35.56
	D	65.23	-12.43	-23.18	17.78
D-Flow	L	96.30	-18.51	-30.83	27.78
	D	72.08	-12.61	-24.95	17.78
PPFlow	L	10.15	-8.93	-13.14	8.89
	D	9.1	-9.05	-12.17	13.33
PepGLAD(ideal)	L	83.05	-14.77	-27.65	32.22
	D	77.92	-13.97	-29.25	28.89
PepMirror(cross)	L	95.98	-23.27	-40.66	61.11
	D	90.88	-19.90	-36.07	47.78
PepMirror(triple)	L	96.48	-23.49	-40.80	58.89
	D	91.42	-20.37	-36.51	45.56
PepMirror(commu.)	L	97.23	-24.01	-41.25	60.00
	D	91.13	-20.31	-36.34	42.22

B. Theory Details

B.1. Finding axial vector features via decomposition of the tensor product of $SO(3)$ representations

This subsection recaps the minimal $SO(3)$ representation theory we use and uses the concrete Cartesian formulas that yield the dot product, cross product, and the symmetric-traceless tensor $M(u)$. We then explain how our three axial features are obtained by composing these low-order geometric components.

Basic notation for $SO(3)$ representations. Let $SO(3)$ act on $V := \mathbb{R}^3$ by the standard (geometric) action $v \mapsto Rv$. This 3-dimensional representation is the irreducible representation of angular momentum index $l = 1$, commonly denoted $V^{(1)}$ ($\dim V^{(\ell)} = 2\ell + 1, \ell \geq 0$). For any two representations U, W of $SO(3)$, the tensor-product representation $U \otimes W$ is defined by

$$R \cdot (u \otimes w) := (Ru) \otimes (Rw), \quad \forall R \in SO(3), u \in U, w \in W, \quad (21)$$

extended linearly.

A fundamental problem in representation theory is to decompose the tensor products into irreducible representations. The Clebsch-Gordan decomposition (see (Fulton & Harris, 2004; Hall, 2015), or (Thomas et al., 2018) for a machine learning perspective) is such a result: for irreducible representations $V^{(\ell_1)}$ and $V^{(\ell_2)}$,

$$V^{(\ell_1)} \otimes V^{(\ell_2)} \cong \bigoplus_{J=|\ell_1-\ell_2|}^{\ell_1+\ell_2} V^{(J)}. \quad (22)$$

In particular,

$$V^{(1)} \otimes V^{(1)} \cong V^{(0)} \oplus V^{(1)} \oplus V^{(2)}. \quad (23)$$

Cartesian realization via rank-2 tensors. Identify $V \otimes V$ with the space of rank-2 Cartesian tensors (matrices) by

$$\Phi : V \otimes V \rightarrow \mathbb{R}^{3 \times 3}, \quad \Phi(u \otimes v) = uv^\top. \quad (24)$$

Under this identification, the $SO(3)$ action becomes conjugation $A \mapsto RAR^\top$. A convenient explicit realization of the three irreducible summands in (23) is given by the classical decomposition of a rank-2 tensor $T_{ij} = u_i v_j$ into (i) scalar representation, (ii) vector representation, and (iii) traceless symmetric tensor representation; see, e.g., the formulas

summarized in (Foster, 2021):

$$\text{(scalar, } l = 0) \quad \mathcal{P}_0(T) := T_{kk} = u \cdot v, \quad (25)$$

$$\text{(vector, } l = 1) \quad (\mathcal{P}_1(T))_i := \epsilon_{ijk} T_{jk} = (u \times v)_i, \quad (26)$$

$$\text{(traceless sym., } l = 2) \quad (\mathcal{P}_2(T))_{ij} := \frac{1}{2}(T_{ij} + T_{ji}) - \frac{1}{3}\delta_{ij}T_{kk}, \quad (27)$$

where we employ the Einstein summation convention throughout, and ϵ_{ijk} is the Levi-Civita symbol, which is antisymmetric in all indices with $\epsilon_{123} = 1$, \mathcal{P}_i is the component-extraction map. Equations (25)–(27) realize the decomposition (23) in a basis-free Cartesian form: \mathcal{P}_0 extracts the $l = 0$ component, \mathcal{P}_1 extracts the $l = 1$ component, and \mathcal{P}_2 extracts the $l = 2$ component.

The symmetric–traceless tensor $M(u)$. As another geometric component, specializing (27) to $u = v$ yields the standard traceless symmetric tensor

$$M(u) := \mathcal{P}_2(u \otimes u) = uu^\top - \frac{1}{3}\|u\|^2 I. \quad (28)$$

This tensor carries the $l = 2$ irreducible representation $V^{(2)}$.

From low-order components to our three axial features. In our model, the input provides multiple $l = 1$ vector channels; denote three such polar vector channels by $u, v, w \in \mathbb{R}^3$. The decomposition above provides two key geometric building blocks: (i) the $l = 1$ coupling $u \times v$ from (26), and (ii) the $l = 2$ object $M(u)$ from (28). We then form three (axial) vector features by simple compositions of these primitives:

$$\mathbf{f}_1 := u \times v, \quad (29)$$

$$\mathbf{f}_2 := ((u \times v) \cdot w) w, \quad (30)$$

$$\mathbf{f}_3 := \text{ax}([M(v), M(u)]) = (u \cdot v)(u \times v), \quad (31)$$

where $[A, B] = AB - BA$ is the matrix commutator and $\text{ax}(\cdot)$ maps an antisymmetric matrix A to its axial vector $a \in \mathbb{R}^3$ defined by $A_{ij} = \epsilon_{ijk} a_k$.

Feature \mathbf{f}_1 captures the oriented normal of the (u, v) -plane. \mathbf{f}_2 injects signed-volume information via the scalar triple product. \mathbf{f}_3 vanishes when $u \perp v$ or $u \parallel v$, encoding a distinct coupling between u and v . In practice, for numerical stability in the deep Neural Network, we use normalization in some channels, see Alg. 1 for AFI implementation of the above three axial vector features.

Remark B.1. In principle, one can construct infinitely many axial vector features from polar vector channels by composing higher-order tensor products and contractions. In practice, we use only the three low-order features above for their computational efficiency and ease of implementation. Our construction is not intended to enumerate all possible axial features, nor to claim optimality.

B.2. Equivariance proof

proof of Proposition 3.5. It is direct to check the parity of axial features: if we reflect $u, v, w \mapsto -u, -v, -w$, the features will not change sign. Since the feature mixing is channel-wise and the polar vector features are $E(3)$ -equivariant, we only need to check the axial features are $SE(3)$ -equivariant. Let $g = (R, t) \in SE(3)$ with $R \in SO(3)$. The three features are built from *vector* inputs u, v (and possibly w), translations do not act on these vectors since the initialization (embedding) of the input molecules uses the differences of vectors (Jiao et al., 2024; Kong et al., 2025b), we only need to check $SO(3)$ -equivariance. We write $g \cdot u := Ru$.

(1) Cross product. Define $\mathbf{f}_1(u, v) := u \times v \in \mathbb{R}^3$. For any $R \in SO(3)$ and any $x \in \mathbb{R}^3$,

$$x \cdot ((Ru) \times (Rv)) = \det[x, Ru, Rv] = \det[R^\top x, u, v] = (R^\top x) \cdot (u \times v) = x \cdot R(u \times v),$$

where we used the scalar triple product identity $a \cdot (b \times c) = \det[a, b, c]$ and $\det R = 1$. Since this holds for all x , we get

$$(Ru) \times (Rv) = R(u \times v),$$

Algorithm 1 Axial Feature Injection (AFI).

Note: The `if/else` structure is for illustrative purposes only. In implementation, each `TYPE` should be compiled into a separate function or module to eliminate runtime branching and ensure efficient execution.

Input: polar ($E(3)$ -equivariant) vector channels $V \in \mathbb{R}^{N \times 3 \times K}$

Output: polar-axial mixing (only $SE(3)$ -equivariant) vector channels $\tilde{V} \in \mathbb{R}^{N \times 3 \times K}$

Parameters: an unbiased linear layer `Linear`: $\mathbb{R}^{2K} \rightarrow \mathbb{R}^K$ applied along the channel dimension

Choice: axial vector feature `TYPE` $\in \{\text{CROSS}, \text{TRIPLE}, \text{COMMUTATOR}\}$

Channel shift (wrap-around) and normalization:

$V^{(1)} \leftarrow \text{roll}(V, -1, \text{dim} = -1)$ (next channel)

$\hat{V}^{(1)} \leftarrow \text{normalize}(V^{(1)}, \text{dim} = -2, \text{keepdim} = \text{True})$ (normalize to unit vector in \mathbb{R}^3)

Construct axial channels $A \in \mathbb{R}^{N \times 3 \times K}$:

if `TYPE` = `CROSS` **then**

$A \leftarrow \text{cross}(V, \hat{V}^{(1)}, \text{dim} = -2)$

else if `TYPE` = `TRIPLE` **then**

$V^{(2)} \leftarrow \text{roll}(V, -2, \text{dim} = -1)$ (next-next channel)

$\hat{V}^{(2)} \leftarrow \text{normalize}(V^{(2)}, \text{dim} = -2, \text{keepdim} = \text{True})$

$C \leftarrow \text{cross}(V, \hat{V}^{(1)}, \text{dim} = -2)$

$s \leftarrow \text{dot}(C, \hat{V}^{(2)}, \text{dim} = -2, \text{keepdim} = \text{True})$

$A \leftarrow s \odot \hat{V}^{(2)}$

else if `TYPE` = `COMMUTATOR` **then**

$V_{\text{norm}} \leftarrow \text{normalize}(V, \text{dim} = -2, \text{keepdim} = \text{True})$

$s \leftarrow \text{dot}(V_{\text{norm}}, \hat{V}^{(1)}, \text{dim} = -2, \text{keepdim} = \text{True})$

$C \leftarrow \text{cross}(V, \hat{V}^{(1)}, \text{dim} = -2)$

$A \leftarrow s \odot C$

end if

Inject axial information by channel mixing:

$Z \leftarrow \text{Concat}(V, A; \text{dim} = -1) \in \mathbb{R}^{N \times 3 \times 2K}$

$\tilde{V} \leftarrow \text{Linear}(Z)$ (applied to the last dimension, no bias)

return \tilde{V}

i.e. \mathbf{f}_1 is $SO(3)$ -equivariant (hence $SE(3)$ -equivariant).

(2) Scalar triple product times a vector. Let $\tau(u, v, w) := w \cdot (u \times v) \in \mathbb{R}$ and define the vector feature

$$\mathbf{f}_2(u, v, w) := \tau(u, v, w) w = (w \cdot (u \times v)) w \in \mathbb{R}^3.$$

Using the same determinant identity and $\det R = 1$,

$$\tau(Ru, Rv, Rw) = (Rw) \cdot ((Ru) \times (Rv)) = \det[Rw, Ru, Rv] = \det[w, u, v] = \tau(u, v, w),$$

so τ is $SO(3)$ -invariant. Therefore

$$\mathbf{f}_2(Ru, Rv, Rw) = \tau(Ru, Rv, Rw) (Rw) = \tau(u, v, w) R w = R \mathbf{f}_2(u, v, w),$$

so \mathbf{f}_2 is $SO(3)$ -equivariant (hence $SE(3)$ -equivariant).

(3) Commutator feature via traceless rank-2 tensors. Let

$$M(u) := uu^\top - \frac{1}{3}\|u\|^2 I \in \mathbb{R}^{3 \times 3}.$$

Define

$$\mathbf{f}_3(u, v) := \text{ax}([M(v), M(u)]) = \text{ax}([vv^\top, uu^\top]).$$

For any $x \in \mathbb{R}^3$,

$$[vv^\top, uu^\top]x = v(v^\top u)(u^\top x) - u(u^\top v)(v^\top x) = (u \cdot v)(v(u \cdot x) - u(v \cdot x)).$$

Using the vector triple product identity $(a \times b) \times x = b(a \cdot x) - a(b \cdot x)$, we get

$$v(u \cdot x) - u(v \cdot x) = (u \times v) \times x,$$

so

$$[vv^\top, uu^\top]x = (u \cdot v)(u \times v) \times x.$$

Therefore $[vv^\top, uu^\top]$ is the cross-product matrix of the axial vector

$$(u \cdot v)(u \times v),$$

which is equivalent up to the convention of the hat map (i.e., $\widehat{\omega}x = \omega \times x$). We obtain $\mathbf{f}_3(u, v) = (u \cdot v)(u \times v)$. Therefore, since $(Ru) \cdot (Rv) = u \cdot v$ and $(Ru) \times (Rv) = R(u \times v)$ (by part (1)),

$$\mathbf{f}_3(Ru, Rv) = ((Ru) \cdot (Rv))((Ru) \times (Rv)) = (u \cdot v)R(u \times v) = R\mathbf{f}_3(u, v),$$

so \mathbf{f}_3 is $SO(3)$ -equivariant.

Combining the three parts, all listed features are $SE(3)$ -equivariant with respect to (u, v) (and w in (2)).

□

B.3. Chirality awareness with AFI

B.3.1. SETUP AND NOTATION.

Fix a sample X and consider a fixed node index $i \in \{1, \dots, N\}$ and an output channel index $k \in \{1, \dots, K\}$. Throughout Appendix B.3, $H(X)$ and $V(X)$ refer to the intermediate features before the channel-wise MLP φ . In particular, we write

$$V_i(X) = (v_{i,1}(X), \dots, v_{i,K}(X)), \quad v_{i,k}(X) \in \mathbb{R}^3,$$

for the polar vector channels at this stage (i.e., *before* the feature mixing at the end of this block).

Based on the polar vector features, we also construct axial vector feature channels like 3.3,

$$A_i(X) = (a_{i,1}(X), \dots, a_{i,K}(X)), \quad a_{i,k}(X) \in \mathbb{R}^3,$$

computed from the same post-attention, pre-FFN representations.

By definition, polar vectors change sign while axial vectors do not:

$$v_{i,k}(-X) = -v_{i,k}(X), \quad a_{i,k}(-X) = a_{i,k}(X), \quad k = 1, \dots, K. \quad (32)$$

B.3.2. LINEAR FEATURE MIXING

Let $A_k, B_k \in \mathbb{R}^K$ be channel-wise mixing coefficients (corresponding to the channel-mixing linear map applied after concatenating (v, a)).

To quantify the typical discrepancy behavior, we introduce a mild distributional assumption on the mixing coefficients (A_k, B_k) . Our arguments only require that the coordinates are *independent sub-Gaussian* for concentration. For notational convenience and to keep constants explicit, we state the assumption in the Gaussian case. The same proof extends verbatim to any independent sub-Gaussian distributions with comparable parameters (For example, bounded valued distributions).

Assumption B.2 (Mixing coefficients distribution). For every $k = 1, \dots, K$, A_k and B_k are independent Gaussian vectors

$$A_k \sim \mathcal{N}(0, \sigma_A^2 I_K), \quad B_k \sim \mathcal{N}(0, \sigma_B^2 I_K),$$

for some $\sigma_A, \sigma_B > 0$.

Define the mixed vector features

$$\tilde{v}_{i,k}(X) := A_k^\top v_{i,:}(X) + B_k^\top a_{i,:}(X) \in \mathbb{R}^3, \quad (33)$$

where $v_{i,:}(X) := (v_{i,1}(X), \dots, v_{i,K}(X))$ and $A_k^\top v_{i,:}(X)$ means the linear combination

$$A_k^\top v_{i,:}(X) = \sum_{\ell=1}^K (A_k)_\ell v_{i,\ell}(X) \in \mathbb{R}^3,$$

and similarly $B_k^\top a_{i,:}(X) = \sum_{\ell=1}^K (B_k)_\ell a_{i,\ell}(X) \in \mathbb{R}^3$.

Note that the scalar part of the latent code is $c(X) = \varphi(H(X), \|\tilde{V}(X)\|)$. Under the central reflection,

$$\varphi(-X) = \varphi([H(X), \|A^\top v(X) + B^\top a(X)\|]) \quad (34)$$

$$\varphi(X) = \varphi([H(X), \|-A^\top v(X) + B^\top a(X)\|]). \quad (35)$$

The key quantity is the parity-induced norm difference

$$\Delta_{i,k}(X) := \left| \|\tilde{v}_{i,k}(X)\| - \|\tilde{v}_{i,k}(-X)\| \right|.$$

Assumption B.3 (Boundedness of vector features). There exist constants $S_v, S_a > 0$ such that for every fixed sample X and node i ,

$$\|v_{i,:}(X)\|_F^2 := \sum_{\ell=1}^K \|v_{i,\ell}(X)\|^2 \leq S_v^2, \quad \|a_{i,:}(X)\|_F^2 := \sum_{\ell=1}^K \|a_{i,\ell}(X)\|^2 \leq S_a^2.$$

Assumption B.4 (Non-degenerate polar-axial correlation). Define the correlation matrix $C = C_i(X) \in \mathbb{R}^{K \times K}$ by

$$C_{k\ell} := \langle v_{i,k}(X), a_{i,\ell}(X) \rangle \quad (1 \leq k, \ell \leq K). \quad (36)$$

Assume

$$\|C\|_F \geq \tau > 0 \quad \text{and} \quad r_{\text{eff}}(C) := \frac{\|C\|_F^2}{\|C\|_{\text{op}}^2} \geq r_0,$$

for some constants $\tau > 0$ and $r_0 \geq 1$. Note that $\|C\|_F^2$ is the square sum of all singular values of C , $\|C\|_{\text{op}}$ is the maximal singular value of C . $r_{\text{eff}}(C)$ is the so-called efficient rank, a quantitative value of the rank of matrix C .

Lemma B.5 (Parity flips only the polar part). *Let*

$$p := A_k^\top v_{i,:}(X) \in \mathbb{R}^3, \quad q := B_k^\top a_{i,:}(X) \in \mathbb{R}^3.$$

Then

$$\tilde{v}_{i,k}(X) = p + q, \quad \tilde{v}_{i,k}(-X) = -p + q.$$

Consequently,

$$\|\tilde{v}_{i,k}(X)\|^2 - \|\tilde{v}_{i,k}(-X)\|^2 = \|p + q\|^2 - \|-p + q\|^2 = 4\langle p, q \rangle, \quad (37)$$

and

$$\Delta_{i,k}(X) = \frac{4|\langle p, q \rangle|}{\|p + q\| + \|q - p\|} \geq \frac{2|\langle p, q \rangle|}{\|p\| + \|q\|}. \quad (38)$$

Proof. The parity rule (32) implies

$$A_k^\top v_{i,:}(-X) = \sum_{\ell=1}^K (A_k)_\ell v_{i,\ell}(-X) = \sum_{\ell=1}^K (A_k)_\ell (-v_{i,\ell}(X)) = -p,$$

while

$$B_k^\top a_{i,:}(-X) = \sum_{\ell=1}^K (B_k)_\ell a_{i,\ell}(-X) = \sum_{\ell=1}^K (B_k)_\ell a_{i,\ell}(X) = q.$$

Thus $\tilde{v}_{i,k}(-X) = -p + q$ and $\tilde{v}_{i,k}(X) = p + q$.

To prove (37), expand both squares:

$$\|p + q\|^2 = \|p\|^2 + \|q\|^2 + 2\langle p, q \rangle, \quad \|-p + q\|^2 = \|p\|^2 + \|q\|^2 - 2\langle p, q \rangle.$$

Subtracting gives $\|p + q\|^2 - \|-p + q\|^2 = 4\langle p, q \rangle$.

For (38), use the identity $|a - b| = \frac{|a^2 - b^2|}{a + b}$ for $a, b \geq 0$:

$$\Delta_{i,k}(X) = \left| \|p + q\| - \|q - p\| \right| = \frac{\left| \|p + q\|^2 - \|q - p\|^2 \right|}{\|p + q\| + \|q - p\|} = \frac{4|\langle p, q \rangle|}{\|p + q\| + \|q - p\|}.$$

Finally, by triangle inequality,

$$\|p + q\| \leq \|p\| + \|q\|, \quad \|q - p\| \leq \|p\| + \|q\|,$$

hence $\|p + q\| + \|q - p\| \leq 2(\|p\| + \|q\|)$, which yields

$$\Delta_{i,k}(X) \geq \frac{4|\langle p, q \rangle|}{2(\|p\| + \|q\|)} = \frac{2|\langle p, q \rangle|}{\|p\| + \|q\|}.$$

□

Lemma B.6 (Small-ball bound for a Gaussian bilinear form). *Let $A \sim \mathcal{N}(0, \sigma_A^2 I_K)$ and $B \sim \mathcal{N}(0, \sigma_B^2 I_K)$ be independent, and let $C \in \mathbb{R}^{K \times K}$ be fixed. Define the bilinear form*

$$S := A^\top C B. \quad (39)$$

Then for any $\varepsilon \in (0, 1)$,

$$\mathbb{P}\left(|S| \leq \varepsilon \sigma_A \sigma_B \|C\|_F\right) \leq \frac{2}{\sqrt{\pi}} \varepsilon + 2 \exp(-c r_{\text{eff}}(C)), \quad (40)$$

where $c > 0$ is an absolute constant and $r_{\text{eff}}(C) = \|C\|_F^2 / \|C\|_{\text{op}}^2$.

Proof. **Step 1 (Condition on A).** Since B is Gaussian and independent of A , then conditioned on A ,

$$S \mid A = A^\top C B \sim \mathcal{N}(0, \sigma_B^2 \|C^\top A\|^2).$$

Let $Z \sim \mathcal{N}(0, 1)$. Then $S \mid A \sim \sigma_B \|C^\top A\| Z$ in distribution. Hence for any $t > 0$,

$$\mathbb{P}(|S| \leq t \mid A) = \mathbb{P}\left(|Z| \leq \frac{t}{\sigma_B \|C^\top A\|}\right) \leq \sqrt{\frac{2}{\pi}} \frac{t}{\sigma_B \|C^\top A\|}, \quad (41)$$

where we used the standard bound for $Z \sim \mathcal{N}(0, 1)$: $\mathbb{P}(|Z| \leq u) \leq \sqrt{\frac{2}{\pi}} u$ for $u \geq 0$.

Step 2 (Lower bound $\|C^\top A\|$ via Hanson-Wright). Write $A = \sigma_A g$ with $g \sim \mathcal{N}(0, I_K)$, and set

$$M := C C^\top \succeq 0.$$

Then

$$\|C^\top A\|^2 = \sigma_A^2 \|C^\top g\|^2 = \sigma_A^2 g^\top (C C^\top) g = \sigma_A^2 g^\top M g. \quad (42)$$

We apply the Hanson-Wright inequality in the Gaussian case (see (Vershynin, 2018) Theorem 6.2.1). In the notation of that theorem:

$$X = g \in \mathbb{R}^K, \quad (\text{mean-zero, independent, sub-Gaussian coordinates with } \|X_i\|_{\psi_2} \lesssim 1), \quad A_{\text{HW}} = M.$$

The theorem states that there exist absolute constants $c, C > 0$ such that for all $t \geq 0$,

$$\mathbb{P}\left(\left|g^\top M g - \text{tr}(M)\right| \geq t\right) \leq 2 \exp\left(-c \min\left\{\frac{t^2}{\|M\|_F^2}, \frac{t}{\|M\|_{\text{op}}}\right\}\right). \quad (43)$$

Here

$$\text{tr}(M) = \text{tr}(C C^\top) = \|C\|_F^2, \quad \|M\|_F = \|C C^\top\|_F, \quad \|M\|_{\text{op}} = \|C C^\top\|_{\text{op}} = \|C\|_{\text{op}}^2.$$

We take $t = \frac{1}{2}\text{tr}(M) = \frac{1}{2}\|C\|_F^2$ in (43). Then

$$\mathbb{P}\left(g^\top M g \leq \frac{1}{2}\text{tr}(M)\right) \leq \mathbb{P}\left(|g^\top M g - \text{tr}(M)| \geq \frac{1}{2}\text{tr}(M)\right) \leq 2 \exp\left(-c \min\left\{\frac{\text{tr}(M)^2}{4\|M\|_F^2}, \frac{\text{tr}(M)}{2\|M\|_{\text{op}}}\right\}\right).$$

Using $\|M\|_F^2 \leq \|M\|_{\text{op}}\text{tr}(M)$ (since $M \succeq 0$), we get

$$\frac{\text{tr}(M)^2}{\|M\|_F^2} \geq \frac{\text{tr}(M)}{\|M\|_{\text{op}}}.$$

Hence the minimum is controlled by the second term, and we obtain

$$\mathbb{P}\left(g^\top M g \leq \frac{1}{2}\|C\|_F^2\right) \leq 2 \exp\left(-c' \frac{\|C\|_F^2}{\|C\|_{\text{op}}^2}\right) = 2 \exp\left(-c' r_{\text{eff}}(C)\right), \quad (44)$$

where $c' = c/2 > 0$ is an absolute constant and $r_{\text{eff}}(C) := \|C\|_F^2/\|C\|_{\text{op}}^2$ is the effective rank. Therefore, defining the event

$$\mathcal{E} := \left\{\|C^\top A\| \geq \sigma_A \|C\|_F / \sqrt{2}\right\},$$

we have from (42) and (44) that

$$\mathbb{P}(\mathcal{E}^c) \leq 2 \exp\left(-c' r_{\text{eff}}(C)\right). \quad (45)$$

Step 3 (Standard conditional small-ball bound). Set $t := \varepsilon \sigma_A \sigma_B \|C\|_F$. On \mathcal{E} we have $\|C^\top A\| \geq \sigma_A \|C\|_F / \sqrt{2}$, thus by (41),

$$\mathbb{P}(|S| \leq t \mid A) \leq \sqrt{\frac{2}{\pi}} \frac{\varepsilon \sigma_A \sigma_B \|C\|_F}{\sigma_B (\sigma_A \|C\|_F / \sqrt{2})} = \frac{2}{\sqrt{\pi}} \varepsilon.$$

Therefore,

$$\mathbb{P}(|S| \leq t) \leq \mathbb{P}(|S| \leq t, \mathcal{E}) + \mathbb{P}(\mathcal{E}^c) \leq \frac{2}{\sqrt{\pi}} \varepsilon + 2 \exp\left(-c r_{\text{eff}}(C)\right).$$

This is exactly (40). □

Lemma B.7 (Gaussian norm bound). *If $G \sim \mathcal{N}(0, I_K)$, then for any $t \geq 0$,*

$$\mathbb{P}(\|G\| \geq \sqrt{K} + t) \leq e^{-t^2/2}.$$

In particular,

$$\mathbb{P}(\|G\| \leq 2\sqrt{K}) \geq 1 - e^{-K/2}.$$

Proof. This is a standard Gaussian concentration bound for the Lipschitz function $g \mapsto \|g\|$ with Lipschitz constant 1. For completeness: by Gaussian isoperimetry (or concentration of measure), $\mathbb{P}(\|G\| \geq \mathbb{E}\|G\| + t) \leq e^{-t^2/2}$. Since $\mathbb{E}\|G\| \leq \sqrt{K}$, we get the displayed inequality. Setting $t = \sqrt{K}$ yields $\mathbb{P}(\|G\| \leq 2\sqrt{K}) \geq 1 - e^{-K/2}$. □

Theorem B.8 (Chirality awareness, discrepancy). *Fix a sample X , node i and channel k . Assume (33) and the parity rule (32). Under Assumptions B.3–B.4, define C by (36). Let $\Delta_{i,k}(X) = \left|\|\tilde{v}_{i,k}(X)\| - \|\tilde{v}_{i,k}(-X)\|\right|$.*

Then for any $\varepsilon \in (0, 1)$, with probability at least

$$1 - \left(\frac{2}{\sqrt{\pi}} \varepsilon + 2e^{-c\varepsilon} + 2e^{-K/2}\right),$$

we have the explicit lower bound

$$\Delta_{i,k}(X) \geq \frac{c_0 \varepsilon \sigma_A \sigma_B \tau}{\sigma_A S_v + \sigma_B S_a}, \quad (46)$$

where $c_0 > 0$ is an absolute constant (one may take $c_0 = \frac{1}{2}$ after absorbing constant factors). In particular, $\Delta_{i,k}(X)$ is bounded away from 0 with high probability.

Moreover, in the absence of AFI (i.e., $B_k \equiv 0$ so that $q = 0$), we have $\Delta_{i,k}(X) = 0$ deterministically.

In the informal version Theorem 3.1, the two constants are

$$\delta_W(\varepsilon) = \frac{2}{\sqrt{\pi}} \varepsilon + 2e^{-c\varepsilon} + 2e^{-K/2}, \quad c_W = \frac{c_0 \sigma_A \sigma_B \tau}{\sigma_A S_v + \sigma_B S_a}.$$

Proof. **Step 1 (Reduce norm separation to an inner product).** By Lemma B.5, for $p = A_k^\top v_{i,:}(X)$ and $q = B_k^\top a_{i,:}(X)$,

$$\Delta_{i,k}(X) \geq \frac{2|\langle p, q \rangle|}{\|p\| + \|q\|}. \quad (47)$$

Step 2 (Express $\langle p, q \rangle$ as a bilinear form). Using linearity and the definition of C in (36),

$$\langle p, q \rangle = \left\langle \sum_{\ell=1}^K (A_k)_\ell v_{i,\ell}(X), \sum_{m=1}^K (B_k)_m a_{i,m}(X) \right\rangle = \sum_{\ell=1}^K \sum_{m=1}^K (A_k)_\ell (B_k)_m \langle v_{i,\ell}(X), a_{i,m}(X) \rangle = A_k^\top C B_k.$$

Therefore, if we set $S := A_k^\top C B_k$,

$$|\langle p, q \rangle| = |S|. \quad (48)$$

Step 3 (Lower bound $|S|$ with high probability). Apply Lemma B.6 to $S = A_k^\top C B_k$. Since $r_{\text{eff}}(C) \geq r_0$ by Assumption B.4, for any $\varepsilon \in (0, 1)$, with probability at least

$$1 - \left(\frac{2}{\sqrt{\pi}} \varepsilon + 2e^{-cr_0} \right), \quad (49)$$

we have

$$|S| \geq \varepsilon \sigma_A \sigma_B \|C\|_F \geq \varepsilon \sigma_A \sigma_B \tau, \quad (50)$$

where the second inequality uses $\|C\|_F \geq \tau$.

Step 4 (Upper bound the denominator $\|p\| + \|q\|$ with high probability). Write $A_k = \sigma_A G_A$ and $B_k = \sigma_B G_B$ with $G_A, G_B \sim \mathcal{N}(0, I_K)$ independent. First, by Cauchy–Schwarz,

$$\|p\| = \left\| \sum_{\ell=1}^K (A_k)_\ell v_{i,\ell}(X) \right\| \leq \sum_{\ell=1}^K |(A_k)_\ell| \|v_{i,\ell}(X)\| \leq \left(\sum_{\ell=1}^K (A_k)_\ell^2 \right)^{1/2} \left(\sum_{\ell=1}^K \|v_{i,\ell}(X)\|^2 \right)^{1/2} = \|A_k\| \|v_{i,:}(X)\|_F.$$

Similarly,

$$\|q\| \leq \|B_k\| \|a_{i,:}(X)\|_F.$$

Hence,

$$\|p\| + \|q\| \leq \|A_k\| \|v_{i,:}(X)\|_F + \|B_k\| \|a_{i,:}(X)\|_F. \quad (51)$$

Now use Assumption B.3 to bound $\|v_{i,:}(X)\|_F \leq S_v$ and $\|a_{i,:}(X)\|_F \leq S_a$:

$$\|p\| + \|q\| \leq \|A_k\| S_v + \|B_k\| S_a.$$

Next, apply Lemma B.7 to G_A and G_B : with probability at least $1 - 2e^{-K/2}$,

$$\|G_A\| \leq 2\sqrt{K} \quad \text{and} \quad \|G_B\| \leq 2\sqrt{K}.$$

On this event,

$$\|A_k\| = \sigma_A \|G_A\| \leq 2\sigma_A \sqrt{K}, \quad \|B_k\| = \sigma_B \|G_B\| \leq 2\sigma_B \sqrt{K},$$

and thus

$$\|p\| + \|q\| \leq 2\sqrt{K} (\sigma_A S_v + \sigma_B S_a). \quad (52)$$

(If one prefers to remove the factor \sqrt{K} , one may instead normalize A_k, B_k at initialization; we keep the explicit dependence here.)

Step 5 (Combine bounds). Intersect the event (50) and the event (52). By a union bound, this intersection holds with probability at least

$$1 - \left(\frac{2}{\sqrt{\pi}} \varepsilon + 2e^{-cr_0} + 2e^{-K/2} \right).$$

On this intersection, substitute (50) into (47) and then use (52):

$$\Delta_{i,k}(X) \geq \frac{2|S|}{\|p\| + \|q\|} \geq \frac{2 \cdot \varepsilon \sigma_A \sigma_B \tau}{2\sqrt{K}(\sigma_A S_v + \sigma_B S_a)} = \frac{\varepsilon \sigma_A \sigma_B \tau}{\sqrt{K}(\sigma_A S_v + \sigma_B S_a)}.$$

This proves (46) up to an absolute constant c_0 (absorbing \sqrt{K} if one uses the normalized convention for A_k, B_k ; otherwise keep the explicit \sqrt{K} factor as above).

Step 6 (No AFI implies no separation). If $B_k \equiv 0$, then $q \equiv 0$ and $\tilde{v}_{i,k}(X) = p$, $\tilde{v}_{i,k}(-X) = -p$. Thus $\|\tilde{v}_{i,k}(X)\| = \|\tilde{v}_{i,k}(-X)\|$ and $\Delta_{i,k}(X) = 0$ deterministically. \square

Corollary B.9 (Chirality awareness, formal). *Assume the latter 2-layer MLP is φ that takes the concatenation*

$$\text{scaler}(X) = [H(X), \|\tilde{v}_{i,k}(X)\|],$$

as input where $H(X)$ is reflection-invariant (depends only on types, distances, dot products, etc.). Assume φ is μ -coercivity in its second argument, i.e.

$$\|\varphi(\text{scaler}(X)) - \varphi(\text{scaler}(-X))\| \geq \mu \cdot \Delta_{i,k}(X),$$

and in particular Theorem B.8 yields a high-probability lower bound on the scalar-output discrepancy. The two constants in 3.1 are

$$\delta_W = \left(\frac{2}{\sqrt{\pi}} \varepsilon + 2e^{-cr_0} + 2e^{-K/2} \right), \quad c_W = \frac{c_0 \mu \sigma_A \sigma_B \tau}{\sigma_A S_v + \sigma_B S_a}.$$

Proof. Since $H(-X) = H(X)$ by parity invariance, the only change in the input to φ comes from the norm term. Applying the coercivity property in that coordinate gives the corollary. \square

Remark B.10. The coercivity assumption is a non-degenerate assumption on φ . It holds for the general Network parameters. One can analyze its derivative and form concentration arguments as above to show that this non-degeneracy is generic.

B.4. Proof of diffusion stability

Proof of Theorem 3.4. Let Z_t, Z'_t solve (16) with the same Brownian motion and the same initial point $Z_T = Z'_T$ with different conditions c, c' .

$$dZ_t = b_\theta(Z_t, t, c) dt + \sigma(t) dW_t, \quad (53)$$

$$dZ'_t = b_\theta(Z'_t, t, c') dt + \sigma(t) dW_t. \quad (54)$$

Set $\Delta_t := Z_t - Z'_t$. Subtraction cancels the noise under coupling, giving

$$d\Delta_t = (b_\theta(Z_t, t, c) - b_\theta(Z'_t, t, c')) dt.$$

Note that for the Euclidean norm, we have $\frac{d}{dt}\|x\| \leq \|\frac{d}{dt}x\|$ by Cauchy Schwarz inequality. Using Assumption 3.3,

$$\frac{d}{dt}\|\Delta_t\| \leq \left\| \frac{d}{dt}\Delta_t \right\| \leq \|b_\theta(Z_t, t, c) - b_\theta(Z'_t, t, c')\| \leq L_z \|\Delta_t\| + L_c \|c - c'\|. \quad (55)$$

Since $Z_T = Z'_T$, we have $\Delta_T = 0$. Applying Grönwall inequality yields

$$\|\Delta_0\| \leq L_c \|c - c'\| \int_0^T e^{L_z s} ds = \frac{L_c}{L_z} (e^{L_z T} - 1) \|c - c'\| := K_{\text{diff}} \|c - c'\|.$$

This provides an explicit coupling (Z_0, Z'_0) of $(\mu_c, \mu_{c'})$ such that $\|Z_0 - Z'_0\| = \|\Delta_0\| \leq K_{\text{diff}} \|c - c'\|$ holds almost surely. By the definition of the Wasserstein metric,

$$W_2(\mu_c, \mu_{c'}) = \inf_{\Gamma(Z_0, Z'_0)} \sqrt{\mathbb{E}\|Z_0 - Z'_0\|^2} \quad (56)$$

$$= \inf_{\Gamma(Z_0, Z'_0)} \sqrt{\mathbb{E}\|\Delta_0\|^2} \leq \frac{L_c}{L_z} (e^{L_z T} - 1) \|c - c'\| \quad (57)$$

where we use a pointwise estimation of the above expectation. We can take $K_{\text{diff}} = \frac{L_c}{L_z} (e^{L_z T} - 1) > 0$. \square

B.5. Initialization: graph embedding

We expand the graph embedding layer of vector features as (Jiao et al., 2024; Kong et al., 2025b). For each node i and channel $k \in \{1, \dots, K\}$, define the edge vector feature

$$Y_{ij,k}(X) := s_{ij,k}(X) (x_i - x_j) \in \mathbb{R}^3, \quad (58)$$

where $s_{ij,k}(X) \in \mathbb{R}$ is a scalar weight depending on the invariant feature (such as atom types) and the RBF of the distance information, and x_i are the 3D coordinates of atom i . We assume the m nearest neighbors of atom i is $\mathcal{N}(i)$. Then the initial vector feature after embedding of node i and channel k is a *polar vector feature*

$$v_{i,k}(X) := \frac{1}{m} \sum_{j \in \mathcal{N}(i)} Y_{ij,k}(X) \in \mathbb{R}^3. \quad (59)$$

C. Experiment Details

C.1. Shape similarity between residue types

To quantify shape similarity between amino acid pairs, we first generate 1,000 conformations per residue type using RDKit and minimize them with the MMFF94s force field. The resulting conformers are clustered with an RMSD threshold of 0.25 Å, and one representative from each cluster is retained to remove redundancy. For residue types i and j , we compute the pairwise shape Tanimoto similarity between every conformer of i and every conformer of j , and apply max pooling to obtain a single similarity score for the pair. Concretely, each conformer pair is first aligned by RDKit O3A with shape-based scoring, after which we compute ShapeTanimotoDist; the similarity is defined as $1 - \text{ShapeTanimotoDist}$.

C.2. Test-Set Preprocessing and Pocket Definition

Because the LNR dataset is curated from the PDB, some entries contain artifacts that can confound parsing and ligand-length determination, including terminal modifications (e.g., N-terminal acetylation and C-terminal amidation), alternative conformations encoded as multiple occupancies (e.g., AGLU/BGLU), and non-protein components such as small molecules, salts, and solvent. To standardize the inputs, we cleaned all structures using Rosetta’s `clean_pdb.py` and performed manual inspection to ensure structural completeness and consistency. The resulting curated set, `LNR_clean`, is used for all downstream evaluations.

Binding pockets within the receptors were defined using a CB distance threshold of <10 Å. For Glycine residues, which lack a natural CB atom, a virtual CB was constructed following previously reported protocols. Since these virtual CB atoms are configured for L-amino acids, we synchronized the pocket residue IDs with those identified in the mirror-image complexes to ensure consistency. To ensure a fair comparison, the same pocket inputs were provided to all evaluated models, unless stated otherwise.

C.3. Training

We largely follow the training protocol of UniMoMo. Specifically, we use the same datasets for linear peptide design (PepBench and ProtFrag) and adopt an identical train/validation split as in UniMoMo. We apply the same two-stage pipeline—training a variational autoencoder (VAE) followed by a latent diffusion model (LDM)—and select the checkpoint with the lowest validation loss for downstream inference and evaluation. All experiments with different axial-vector choices share the same data split and training setup. Detailed hyperparameters are reported in Table S6.

C.4. Inference

Generally, we generated 100 samples for each targets in the LNR test set with the same length as native peptide binders in cleaned complexes. The random seed was set to 12 for reproducing results. After generation, we reconstructed complexes with full-length receptors for downstream analysis. Some model-specific settings are listed below:

RFDiffusion. Among published checkpoints, we employed the `Complex_base_ckpt.pt` for binder design. We found that providing only pocket information leads to pronounced clashes during reconstruction. Therefore, we used full-length structures as input and specify binding sites via hotspots. Following the rule in the training process, we randomly selected 20% pocket residues as hotspot residues for binding site specification, and the same hotspots were used for L and D design.

Table S6. Hyperparameters and settings for training PepMirror and its variants.

Models	UniMoMo(pep.)	PepMirror(cross)	PepMirror(triple)	PepMirror(commutator)
Optimizer	AdamW	AdamW	AdamW	AdamW
β_1	0.9	0.9	0.9	0.9
β_2	0.999	0.999	0.999	0.999
Initial LR	1e-4	1e-4	1e-4	1e-4
LR decay factor	0.8	0.8	0.8	0.8
LR scheduler patience /epochs	5	5	5	5
GPU type	A800	A800	A800	A800
Number of GPUs	8	8	8	8
Days to train (VAE+LDM)	2	2	2	2
Training epochs (VAE)	199	169	179	169
Training epochs (LDM)	375	307	483	448

After generating peptide backbones, we sample 1 sequence using ProteinMPNN with `v_48_020.pt` (48 edges with 0.20 Å noise). Following the procedure described in BindCraft, we set the sampling temperature to 0.0001 to make sampling nearly deterministic, yielding the top-ranked sequence according to the model. After integrating the designed sequence into the ligand, we manually added $C\beta$ atoms for all non-Gly residues to enforce the intended initial chirality. We then kept the receptor side-chain conformations fixed to those of the native receptor, and used PDBFixer and OpenMM to sample and optimize the ligand side-chain conformations. The resulting complexes were subsequently subjected to downstream evaluation.

DiffPepBuilder. Because this model relies on ESM embeddings as sequence representations, we provide full-length structures as input to ensure that the ESM encoding is well-defined and contextually consistent.

PPFlow. We noticed that many designed ligands show severe backbone clashes with receptors, and there is a redock legacy in the released pipeline that heuristically aligns the generated ligand to the native ligand by matching their centroids. However, neither enabling this redocking step nor providing full-length receptor structures could reduce the clash rate. We therefore followed the default setting in the original implementation, using pocket-only inputs without redocking.

PocketXMol. The model generates structures containing non-standard amino acids since it does not group atoms into course-grained tokens. For fair comparison, we only evaluated peptides composed of only canonical residues out of 9,300 generated molecules.

C.5. Implementation of Metrics

Chirality. We calculate the chirality of residues based on the scalar triple product: $T = (\vec{N} - \vec{C}_A) \times (\vec{C} - \vec{C}_A) \cdot (\vec{C}_B - \vec{C}_A)$, where a positive T indicates L and a negative T indicates D. For each tested model, we report the proportion of residues that show desired chirality out of all residues, where glycines that are achiral are excluded. As mentioned below, generated structures were minimized before evaluation, and the desired chirality proportion before and after the minimization are both reported.

Minimization. We minimize the generated complexes using the Amber ff14SB force field. To preserve the generated geometry, we apply harmonic positional restraints to both the receptor and the ligand during minimization, preventing large deviations from the initial model and ensuring that the minimized structures remain representative for evaluation.

Interface Energy. We compute interface energies using AutoDock Vina in score-only mode. Following the UniMoMo definition of interface energy improvement (IMP) (Kong et al., 2025b), we report the proportion of targets for which at least one generated ligand achieves a lower vina score than the reference ligand.

Binding Surface Recovery. We define the binding surface as the set of receptor residues whose $C\alpha$ atoms are within 10, Å of any ligand $C\alpha$ atom. Using the ground-truth complex as reference, we compute for each generated complex the recovery ratio as the fraction of native binding-surface residues that are also present in the generated binding surface.

Diversity. Generally, we define diversity as the number of clusters normalized by the total number of samples. For *sequence diversity*, we cluster the 100 generated sequences for each target independently using complete-linkage hierarchical clustering. For *structure diversity*, we first align complexes by the receptor, then compute pairwise ligand C_α RMSDs, and

perform complete-linkage clustering with a 2, Å cutoff, again separately over the 100 designs generated for each target.

C.6. Design of D-peptide binders against CD38

We used PDB 7DHA as the reference structure, where chain A is the receptor and chain B and C is the binder that define the binding surface. We sampled 5,000 peptides with the length range of [10,12] under a random seed of 12. These generated complexes were minimized under the Amber ff14sb forcefield, and were filtered and ranked based on the following metrics: **Complementary**. We employed Rosetta to calculate the CavityVolume, ShapeComplementary, ElectrostaticComplementary (based on APBS), BuriedHBonds and ExposedHydrophobic, where the latter two are for evaluate the HydrophobicComplementary. **Interactions**. We employed AutoDock Vina to roughly check the binding energy of each interface, and used PLIP to analyze the interactions between targets and binders. In detail, we counted the total number of identified interactions, the number of hydrogen bonds, and the number of mainchain hydrogen bonds. Finally, we utilized FreeSASA to calculate absolute binding surface area (absBSA), and the ratio of absBSA in the SASA of ligands, termed relative BSA (relBSA). **Conservation**. By the PLIP analysis mentioned above, we identified top10 residues of the receptor that participate the most interactions, as well as the proportions of every interaction type for each residue. These residues are termed "hotspots". Then, for each ligand, we checked how many hotspots it covers, and whether the interaction is the most seen type. For comparison, we reported the weighted coverage, where coverage $C = \sum_i w_i \cdot x_i$, where x_i is a hotspot residue, and the weight $w_i = \frac{N(T_{ij})}{\sum_j N(T_{ij})}$, where $N(T_{ij})$ is the number of interactions of type j for hotspot i.

These metrics were divided into two classes. The first class is for filtering out structures that are not reasonable, where we applied thresholds as follows: $\text{absBSA} > 400$, $0.20 < \text{relBSA} < 0.85$, $\text{vina score} < -4.0$, $\text{BuriedHBonds} < 10$, $\text{ShapeComplementary} > 0.65$, $\text{ElectrostaticComplementary} > 0.65$, $\text{TotalInteraction} > 8$, $\text{TotalHBond} > 3$. In addition, we require CavityVolume and ExposedHydrophobic to fall within the lower 80% of the distribution to exclude interfaces with large voids or excessive exposed hydrophobic patches. The second class is for enriching candidates with high possibility of binding in the top, where we calculate the Zscore of the number of mainchain hydrogen bonds and the weighted hotspot coverage, and ranked structures based on their sum. Finally, the top 6 candidates were subjected to downstream synthesis and analysis.

All peptides are chemically synthesized using the routine Fmoc solid phase peptide synthesis (SPPS) protocol, purified with high-performance liquid chromatography (HPLC), and lyophilized. The target protein CD38 is recombinantly expressed in HEK293F and is purified by affinity chromatography based on Ni-NTA and His-tag.

We then used biolayer interferometry (BLI) to assess binding. Briefly, peptides and target proteins were prepared in BLI buffer (50 mM HEPES, 150 mM NaCl, 0.5% Tween-20, 0.05 mg/mL BSA). Peptides were serially diluted from 200 μM using a 3-fold scheme to obtain six concentrations, and the target protein was used at 20 $\mu\text{g/mL}$. Binding kinetics were quantified by fitting association and dissociation traces to estimate k_{on} and k_{off} , and K_D was computed as $k_{\text{off}}/k_{\text{on}}$. Besides this kinetic estimation, we also performed steady-state analysis by fitting the equilibrium response at each concentration to a 1:1 binding isotherm,

$$\text{Response} = R_{\text{max}} \cdot \frac{\text{conc}}{K_D + \text{conc}}, \quad (60)$$

where conc denotes the peptide concentration and R_{max} is the maximal binding response.

For D-1412, the kinetic fitting yields $K_D = 9.9 \pm 0.2 \mu\text{M}$, while the steady-state analysis gives $K_D = 10.5 \pm 0.6 \mu\text{M}$, demonstrating good agreement between the two estimation procedures. For the other 11 candidates, 3 show weak responses but lack enough confidence to claim binding.